NTNU
Norwegian University of
Science and Technology

Effect of Germanium in Silicon for Solar Applications

Giuseppe De Martino

Innovative Sustainable Energy Engineering
Submission date: June 2016
Supervisor: Ursula Gibson, IFY
Co-supervisor: Marisa Di Sabatino, IMT

Norwegian University of Science and Technology
Department of Physics

Not only are we, and with us all the animals and plants of earth, the offspring of the sun; not only is our whole life, from the cradle to the grave and beyond to our final mouldering, a solar transformation; but everything we possess, the civilization we have created, the technique we have invented, are solar gifts.

- Desiderius Papp, Creation's Doom.

Abstract

In this thesis the effect of germanium in silicon for solar applications is studied through the characterization and analysis of two types of samples: multi-crystalline (mc) ingots and microwire arrays. A p-type mc-Si ingot and a p-type mc-SiGe ingot, with 1% of Ge concentration, were cast in the same conditions using the vertical gradient freeze method. The ingots were then vertically and horizontally cut in wafers for the experiments. The microwires were produced employing the molten core fiber drawing method and are composed of a SiGe core, with 6% of Ge concentration, embedded in a silica cladding. Some of the microwires were further treated through a CO_2 laser annealing process, homogenizing the Ge concentration in the core. The Ge concentration variation in the SiGe ingot, experimentally determined using glow discharge mass spectrometry, was in good agreement with the theoretically calculated trend. Fourier transform infrared spectroscopy was performed to evaluate the presence of interstitial oxygen and substitutional carbon in the vertically cut wafers. From these experiments carbon was estimated to exceed the solubility limit in both ingots. The SiGe ingot was found to have higher metallic impurity concentration at the bottom, lower interstitial oxygen and lower substitutional carbon compared to the Si one. These three results were connected to precipitation mechanisms caused by the presence of Ge-vacancy complexes. The Ge-vacancy defect formation was discussed in terms of released strain energy imposed by the larger radius of Ge atoms compared to the Si atoms. Regarding electrical properties, four point probes resistivity measurements on horizonally cut wafers have shown a good agreement between the experimental values and the boron density intentionally added during the casting process. Transmittance and absorption measurements were finally performed on both mc wafers and microwires. A slight increase of light absorption in the infrared region was shown in the SiGe wafers compared to the Si one, due to the change in energy bandgap. Homogeneous and inhomogeneous compositions in the microwires were found considering the polished longitudinal section of their core, with images obtained by scanning electron microscopy. The absorption spectra analysis of the microwires revealed that inhomogeneous samples are absorbing more light in the infrared region and reach the absorption peak more slowly. This behavior was explained in terms of the energy bandgaps variations in the different regions of the inhomogeneous core. These results highlight that SiGe alloy is a valuable solution to increase absorption of light and to reduce impurity levels in silicon based solar cells. Furthermore, the inhomogeneous microwires have shown promising properties that can be used as a starting point for future solar cell systems to reduce the material usage while maintaining high light absorption.

Preface

This master's thesis was written as the conclusion of my master's degree in Innovative Sustainable Energy Engineering at the Technical University of Denmark and the Norwegian University of Science and Technology. The thesis work was done at the Department of Physics and the Department of Materials Science during the spring of 2016 under the supervision of professor Ursula Gibson and co-supervision of Marisa Di Sabatino. First of all I would like to express my sincere gratitude to Ursula Gibson and Marisa Di Sabatino for their support with the project. Our meetings and email conversations have been of fundamental importance for the development of this thesis. It was a pleasure working with you.

I would also like to thank Antoine Autruffe for helping me from the beginning, with the ingots casting, to the end, sharing his ideas on the experimental results. Your collaboration was invaluable. I thank also Eric Karhu, Per Magnus Walmsness and Seunghan Song for making the laboratory a better place to work in and share thoughts. NTNU glass shop, VARIO Kristallbearbeitung and NanoLab staff are acknowledged for their assistance.

Finally I would like to thank my family, my girlfriend Viviana and my friends for their love and patience.

Thank you also to Mac DeMarco, Nick Drake, Tame Impala, Morphine and Bad Liquor Pond for accompanying me during my writing moments.

Contents

List of Abbreviations

ASTM	American Society for Standard Materials
BSE	Back Scattered Electrons
CB	Conduction Band
CZ	Czochralski
DC	Direct Current
DIN	Deutsche Industrial Norms
DL	Detection Limit
DSP	Double Side Polished
EHP	Electron Hole Pair
FPP	Four Point Probes
FTIR	Fourier Transform Infrared
GDMS	Glow Discharge Mass Spectrometry
HV	High Voltage
IBR	Ion Beam Ratio
IR	Infrared
LID	Light Induced Degradation
mc	multi-crystalline
mono	mono-crystalline
NIR	Near Infrared
PDMS	Polydimethylsiloxane
PV	Photovoltaic
RSF	Relative Sensitivity Factor
SD	Standard Deviation
SEM	Scanning Electron Microscope
VB	Valance Band
VGF	Vertical Gradient Freeze

1

Introduction

1.1 Motivation

The exponential growth of energy consumption and the global warming due to burning of fossil fuels have lead to a new public awareness about energy sources, driving renewable energies inside the energy market. Photovoltaic (PV) cells are already a leading technology in their field with 178 GW of global installed capacity in 2014 [1]. Among all the different solutions to produce electricity from solar radiation, silicon based cells are by far the most utilized with 90% of the market share [1]. Even if Si is the most used material, it is not an ideal semiconductor for solar applications [2]. Through a detailed balance efficiency Shockley and Queisser, in 1961 [3], calculated the theoretical efficiency limit for a one bandgap solar cell to be 33% when the energy gap of the material is 1.4 eV. Silicon, with a bandgap of 1.1 eV, is not far from the optimal point but what actually penalizes it is the indirect bandgap. In an indirect semiconductor, as a matter of fact, there is a lower probability for the incoming photons to be absorbed. From a materials point of view this reduced absorption leads to an increase of the required wafer thickness in order to have a sufficient photovoltaic conversion. For example it takes only 1 μm of GaAs (a direct semiconductor) to reach 90% light absorption, versus 100 μm of Si [2]. Furthermore, thicker wafers require higher crystal quality and extremely pure Si, around 99.99999%, to maintain low energy losses in the material. Apart from all these issues, Si is still the leading material for solar cells applications. It has a predominant position due to its abundance in the earth's crust and, most of all, because its production chain was already developed before the advent of PV as a commercial product [2]. High quality Si was indeed produced in large quantities for the microelectronics market. On these basis, it is not surprising that most of the solar cell research efforts are spent trying to discover new suitable materials and geometries, to increase the usable yield of light spectrum while reducing material usage and costs [2].

1.1.1 Silicon-Germanium Alloy

The ideal semiconductor material for photovoltaic applications should have a direct bandgap between 1.1 and 1.9 eV, a reliable and cheap chain production, non toxic features, good photovoltaic conversion efficiency and long term stability. Despite having a slightly smaller bandgap, Silicon-Germanium (SiGe) alloy stands in this research as a good compromise between the already established silicon production chain and the new material properties. Currently its success lies in microelectronics devices, amplifiers in portable equipment such as cellular phones or GPS trackers, in high-performance test instrumentation, and in laser controllers for data storage systems [4]. Si_xGe_{x-1} alloy was first investigated by Stöhr and Klemm in 1939 [5] and found to be a fully miscible alloy. Nevertheless, it is since the quite recent discovery of bandgap tailoring by strain engineering [6], that this alloy has gained a new scientific attention. The possibility to engineer bandgap and lattice parameters, changing the material composition and strain, opens a variety of possible technological solutions, making SiGe appealing for several semiconductor applications. Tuning the bandgap can improve the absorption of light in solar cells. The introduction of Ge, with its lower bandgap, can extend the solar radiation absorption to the infrared region. Modification of the lattice parameters can be used to match other materials lattice constants and create a perfect substrate layer in tandem cells [6]. Local strains in the crystal due to Ge atoms can, instead, be used to modify the presence and distribution of point defects, changing the material interaction with impurity atoms [7].

1.1.2 Microwire-based Solar Cells

Microwire-based solar cell technology is also a promising solution to the described problems of photovoltaic systems based on silicon wafers: light absorption, purity requirements and raw material usage. Microwire solar cells are based on an array of semiconductor wires that can be aligned in two main ways: vertically or horizontally. Vertical wire arrays are an attractive alternative because they can possess both long optical paths, for efficient light absorption, and short transport distances to ensure efficient collection of the photogenerated carriers [8]. The long absorption depth of Si, due to its indirect bandgap, can be developed in the vertical direction, while the collection efficiency, dependent on the wire diameter, can be maintained with lower purity requirements; varying the fiber diameters also allows to reduce the material usage. Horizontally aligned wires arrays can not count on the principle just explained but are easier and cheaper to produce and, using adequate light trapping systems, they can achieve high efficiency [9].

1.2 Previous Research and Overview

In this thesis both SiGe alloy and microwires technology are examined in solar applications. The concept of improving the material properties of silicon solar cells

introducing a small percentage of Ge in the Si melt has been studied in both monocrystalline (mono-Si) and multi-crystalline (mc-Si) cases, but with different focuses. In mono-Si ingots, Ge doping has been analyzed as a possible solution to reduce oxygen impurities, which are one of the main causes of defects during the Czochralski (CZ) solidification process [7] [10]. On the other hand, since mc-Si can be grown by low-cost casting methods like directional solidification it would be ideal to improve the overall conversion efficiency without high increase of the production costs. SiGe has therefore gained interest, in mc-Si research, due to its capacity of improving the material quality, through local strain [11], and light absorption (photocurrent), trough micro-compositional variations [12]. The present work aims to combine these lines of research in order to give an overview of how germanium is affecting the material properties of silicon and how this modifications can be used in multi crystalline and microwires solar cells.

In their work Pan et al. [13] found that light absorption in mc-SiGe is superior to mc-Si solar cells when the average Ge composition is smaller than 5%. Therefore in this thesis a comparison between a mc-Si ingot and a mc-SiGe with 1% of Ge, cast in the same conditions, is carried out. Fourier Infrared Spectroscopy (FTIR) and Glow Discharge Mass Spectrometry (GDMS) are used to study the influence of Ge on the distribution and concentration of impurities. FTIR measurements are particularly focused on study if the reduction of interstitial oxygen, reported by Arivanandhan et. al [7], is developed also in mc-Si, while GDMS is finalized to analyze the variation of metallic impurities behavior in the two ingots. The electrical properties differences are considered through resistivity measurements using the Four Point Probe (FPP) method. Finally transmittance and absorption are measured using a spectrophotometer and an integrating sphere. These optical measurements are performed to study the difference in response of Si versus SiGe ingots and homogeneous vs not homogeneous microwire arrays. The latter comparison is meant to assess if the assumption of Nakajima et al. [14], that micro-compositional variations of Ge in SiGe lead to higher absorption of light than homogeneous SiGe, is verified also in the microwires case. The analyzed microwires are made of a SiGe alloy core with a silica (SiO_2) cladding, produced using the molten core fiber drawing method.

First of all a theoretical part on solar cells physics, solidification and characterization techniques is carried out to set the basis for the experiments analysis. In the following chapter the samples used and the experimental setups are described in order to ensure their reproducibility. The results and discussion chapter is then developed from the comparison between experimental values collected in this thesis and previous research findings. Finally the conclusion and an outlook to future research are proposed.

2

Theory

This chapter will introduce the theoretical background necessary to understand the results and discussion of the experiments in the thesis. First the basis on the working principles of solar cells and semiconductor physics are explained. Then an overview of silicon crystal defects and the definition of the structural defects analyzed in this project are carried out. The third part will describe the solidification theory with special attention to SiGe alloy and metallic segregation. Finally the characterization techniques used, their components and their working principles are illustrated.

2.1 Semiconductor Physics and Solar Cells

Solar photovoltaic energy conversion is a one step conversion process which generates electrical energy from light energy [15]. It relies on concepts of quantum mechanics theory in which light is described as a flux of *photons*, elementary particles carrying energy, according to the equation:

$$E_{photon} = h\nu = \frac{hc}{\lambda} \tag{2.1}$$

where h is the Plank constant, c is the speed of light and λ and ν are the wavelength and frequency of the incoming light.

2.1.1 Band Theory

When many atoms are brought together in a solid, their energy levels splits forming essentially continuous bands of energies [16]. According to this theory the electrons in the crystal lattice are forced to occupy well defined energy bands related to their molecular bonding and lattice periodicity. Every material has its own particular energy band structure and this variety is responsible for the wide range of different electrical characteristics observed experimentally. Considering the highest filled band, called *Valence Band* (VB) and the lowest empty band, called *Conduction Band* (CB), it is possible to distinguish metals, semiconductors and insulators.

Metallic materials have bands that either overlap or are only partially filled and electrons are able to move freely in the crystal lattice. In insulators and semiconductors instead the CB is totally empty and a forbidden region, the *band gap* (E_g), separates it from the VB. Since the VB is totally filled, the CB is empty and there can not be charge transport without empty energy states in which the electrons can move, both insulators and semiconductors have high resistivity at 0 K. What differentiates them is the width of E_g. In semiconductors this energy gap is small enough, 0.5 eV $\leq E_g \leq$3 eV [15], to allow for excitation of electrons from the VB to the CB by a reasonable amount of thermal or optical energy.

The semiconductors behavior of interest in solar cells technology can be understood by considering VB, CB and E_g. Using atoms periodicity in the crystal it is possible to simplify quantum mechanical calculations of the energy states [15], for this reason in the band diagrams the energy is plotted against the wave vector k of the space-dependent wave function in important crystal directions [16], see figure 2.1. For materials with CB minimum and VB maximum occurring at the same k value, which are called *direct semiconductors*, a photon of energy E_g is sufficient to promote an electron from VB to CB. In silicon, which is instead an *indirect semiconductor*, this condition is not fulfilled and a change in momentum is necessary for the electronic transition, see figure 2.1. The momentum variation can be provided by a *phonon*, defined as a collective vibration of atoms [16], but it makes light absorption probability much lower for this kind of materials.

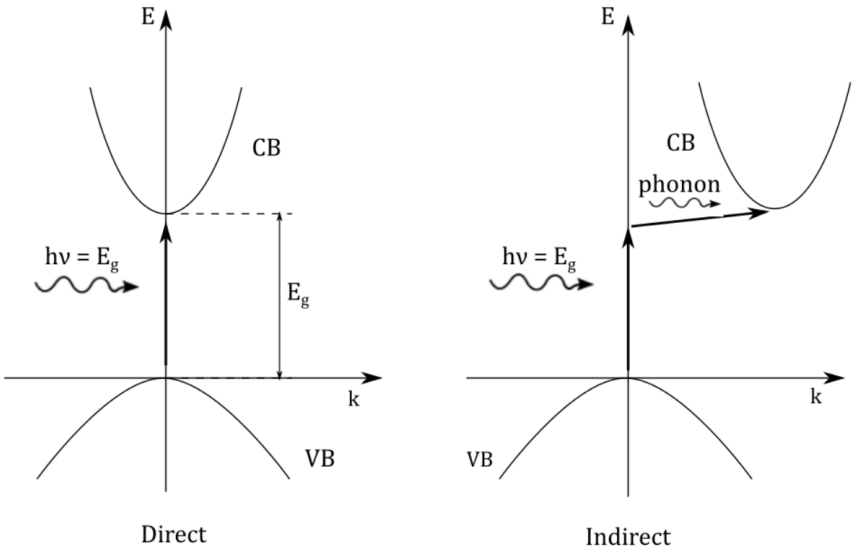

Figure 2.1: *Direct and indirect transitions. On the left a direct semiconductor and on the right an indirect semiconductor band diagram.*

Considering equation 2.1 it is possible to connect light spectrum and energy band gap. Since each frequency is related to a certain energy and the material will absorb photons with $E_{photon} \geq E_g$, then the band gap represents a minimum absorption threshold. Looking at the spectrum in figure 2.2 it is noticeable that, on the right

side of the threshold, a large part of the infrared region could be utilized, decreasing the band gap of few tenths of eV. For this reason, in Si based solar cells, reducing the band gap using Ge can improve light absorption [17].

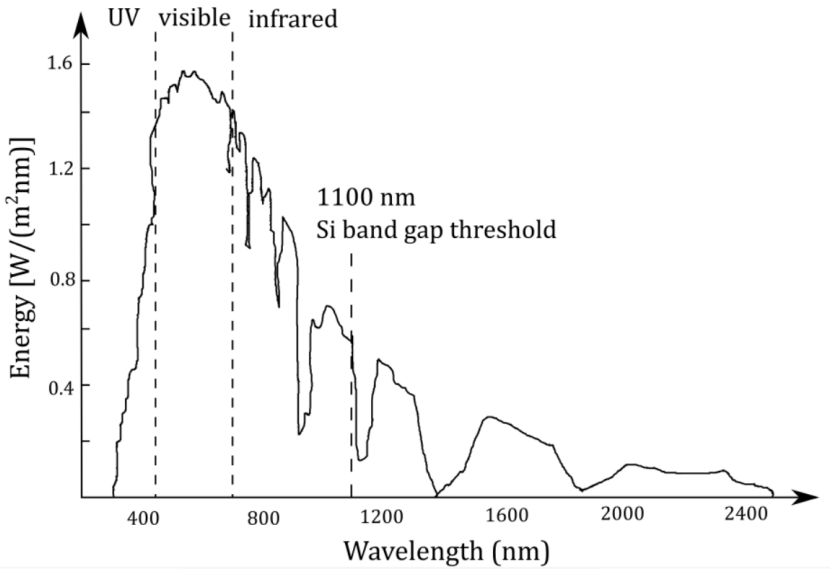

Figure 2.2: *AM 1.5 solar spectrum [18][19] showing the threshold at which Si starts to absorb energy due to its 1.1 eV band gap. The spectrum is also divided in UV, visible and infrared according to the wavelength.*

In order to discuss the influence of impurities in the band structure, it is important to introduce the *Fermi Dirac distribution function*, which gives the probability of occupation of an allowed electron state at any given energy:

$$f(E) = \frac{1}{1 + exp\left(\frac{E-E_F}{k_B T}\right)} \tag{2.2}$$

where k_B is the Boltzmann constant, T is the absolute temperature, E is the given energy and E_F is the *Fermi Level*, which is defined as the energy level where the probability of finding an occupied state is equal to 50%. It can be noticed that at T=0 K the distribution has a simple rectangular shape; see figure 2.3, this implies that all the available states up to E_F are filled with electrons and the ones above E_F are empty. When the temperature increases, according to equation 2.2, there is a finite probability for available energy states higher than E_F to be occupied. In figure 2.3 the Fermi Dirac distribution is represented close to the simplified band diagram, to better visualize when both the probability of occupation and availability of states are present (curve T_2 in figure 2.3): only in that case the electrons can be thermally excited from CB to VB.

From this concept the *electron and hole concentration* is derived and can be calculated as:

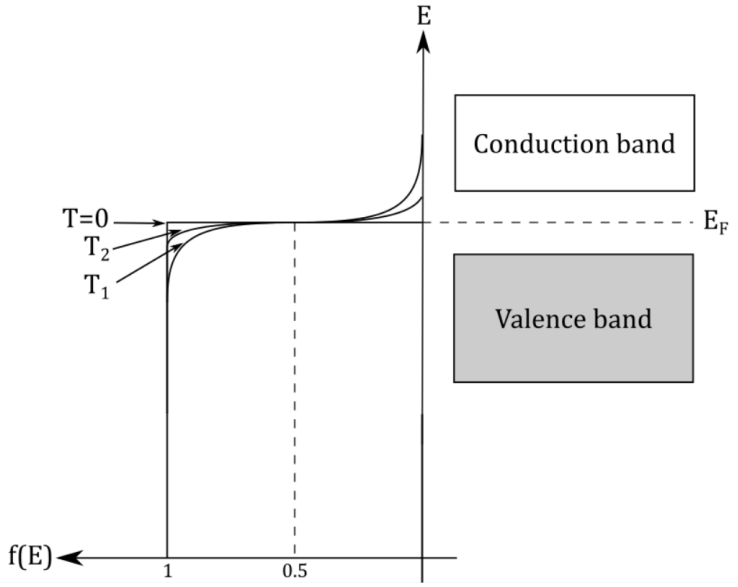

Figure 2.3: *Simplified band diagram and Fermi Dirac distribution for an intrinsic semiconductor at T=0 K, T_1 and T_2 with $T \leq T_1 \leq T_2$.*

$$n_0 = \int_{E_C}^{\infty} f(E)N(E)dE \tag{2.3}$$

where $N(E)dE$ is the density of states in the energy range dE. The subscript 0 used with the electron and hole concentration symbols (n_0,p_0) indicates equilibrium conditions. The same idea is used to calculate p_0 by changing E_C with E_V and $f(E)$ with $1 - f(E)$ in the formula. E_C and E_V are, respectively, the minimum energy of the CB and maximum energy of the VB. The result of an electron excitation (thermal, optical, etc.) is a material with some electrons in an otherwise empty CB and some unoccupied states in an otherwise full VB [16]. This situation is depicted in figure 2.4. It is convenient from now on to consider the empty states in the VB as *holes* (h^+), with positive mass and a positive charge equal to the electron one (e^-). In this way when an electron is promoted to the upper band two charge carriers are generated, they are called the *Electron Hole Pair* (EHP).

2.1.2 Intrinsic and Extrinsic Semiconductors

So far it was always considered an *intrinsic semiconductor* with a perfect crystal and no impurities or defects. If instead this assumption is not fulfilled different bonds are introduced in the crystal lattice and therefore the electron energy states will change [15]. The material is then called *extrinsic semiconductor*. The new energy states caused by impurities will not create almost continuous bands but will be localized. When impurity levels occur within the forbidden energy gap they can modify the

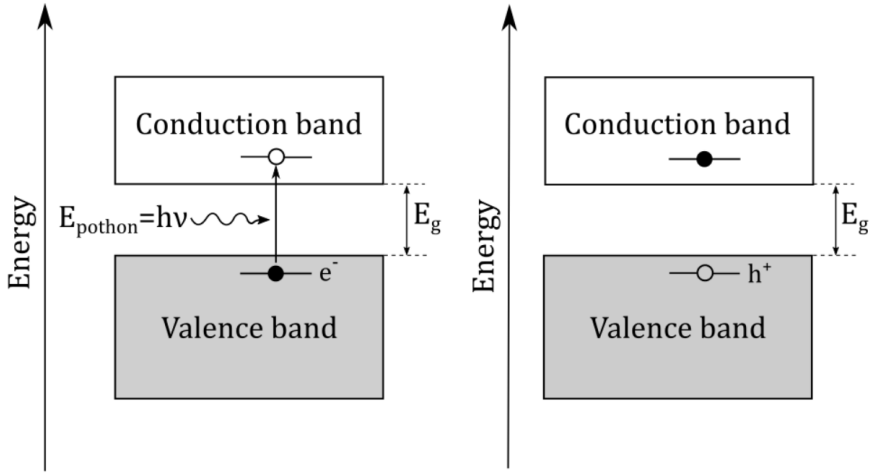

Figure 2.4: *Simplified semiconductor band diagram before and after excitation of an electron by photon absorption. After excitation (figure on the right) the VB is left with a hole of positive charge.*

electronic properties of the material such as the E_F and the concentration of holes and electrons and therefore the conductivity, which is described by the equation:

$$\sigma = q\mu_n n + q\mu_p p \tag{2.4}$$

where q is the electronic charge, μ_n and μ_p are the mobilities of electrons and holes, while n and p are the electrons and holes density. The process of using precise amounts of impurities to engineer the electronic properties of semiconductor materials is defined as *doping*.

Introducing impurity levels close to the VB maximum (E_V in figure 2.5) will decrease the E_F and increase the holes density relative to electrons in thermal equilibrium. These electron energy states are created substituting some of the atoms in the lattice with impurity atoms having one electron less in the valence band. The impurity atoms are called *acceptors* because they subtract one electron from the atomic bonds; the material is then transformed from intrinsic semiconductor to *p-type semiconductor*. Substituting instead the lattice atoms with impurity atoms having one more valence electron will introduce an energy level close to the CB minimum (E_C in figure 2.5) and increase both the E_F and the electron density relative to the holes at thermal equilibrium. Since they donate the excess electron to the lattice these elements are called *donors* and the modified material is called *n-type semiconductor*.

2.1.3 p-n junction

Connecting a p-type material and an n-type material creates a p-n junction. A classical silicon solar cell is essentially a p-n junction built doping the same material

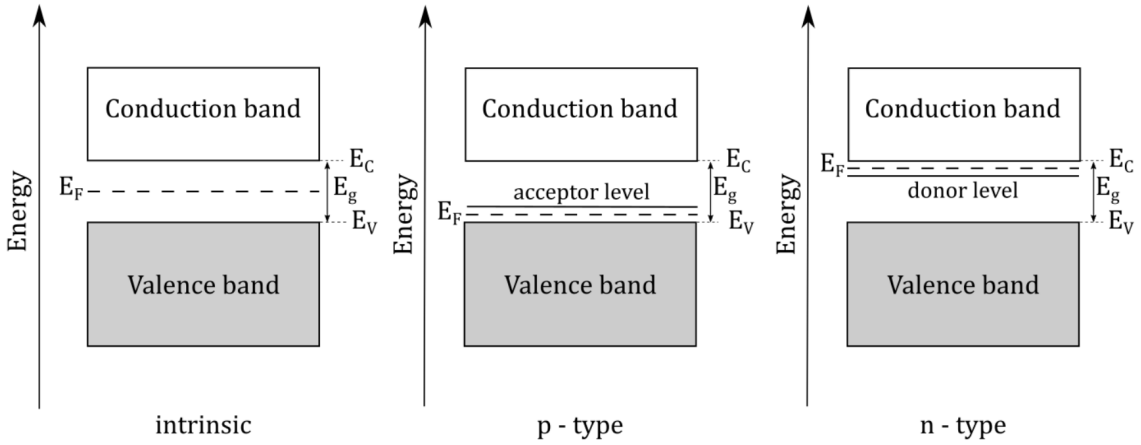

Figure 2.5: *Simplified band diagram of an intrinsic, p-type and n-type semiconductors showing the variation of E_F for the different materials.*

with different atoms in different regions. Since the n-type region has a higher density of electrons, a gradient is established at the junction and electrons will migrate to the p-type region by diffusion. The same is valid for holes which will move in the opposite direction. The diffusion process will leave uncompensated charges on both sides of the junction. The ionized dopant atoms will then set up an electric field opposed to the diffusion mechanism until an equilibrium is reached and no net charge transport is present. At this point the E_F of the two layers are aligned and a contact potential (V_0) is generated, as described in figure 2.6. The region close to the junction is depleted of both electrons and holes presenting a barrier to majority carriers, it is therefore called *depletion region* (W) and the carrier concentration is considered so small that the only contribution to charge density is considered from the ionized dopants [20].

The solar cell device takes advantage of the electric field across the depletion region to separate the photogenerated minority carriers; electrons and holes will move in opposite directions according to their charge, see the red arrows in figure 2.6. If the p-n junction is connected with a circuit to a load, electrons can be extracted from the anode and holes from the cathode. Their energy is used to generate work before they recombine on the other side of the solar cell, closing the circuit.

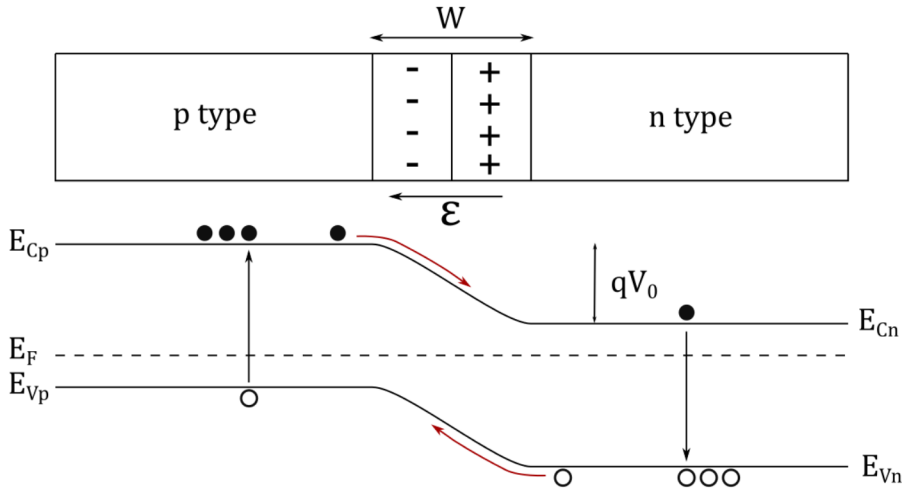

Figure 2.6: *Schematic representation of a p-n junction showing the depletion region W with the uncompensated positive (+) and negative (-) charges. The electric field (ε) goes from the n-type to p-type. Below it the energy bands diagram shows the aligned E_F, the built in voltage (V_0) the photogenerated carriers and their transportation direction of electrons and holes using red arrows.*

2.2 Crystal Defects in Silicon

This section will give a brief overview of imperfections in silicon, introducing terms which will be used later in the discussion of the experimental results.

2.2.1 Structural Defects

Crystalline structures will at any temperature above 0 K contain vacancies or extra atoms and will exhibit a deviation from the ideal structure [21]. Even though it is natural to have these deviations in crystalline compounds, they are called structural defects because the ideal structure is used as reference. Structural defects can be divided according to their dimensionality. Zero dimensional, one dimensional and two dimensional defects are called, respectively, point defects, line defects and planar defects. In this thesis only point defects and grain boundaries are crucial and they will be treated in this chapter.

Point Defects

Point defects are limited to one structural or lattice site and its immediate vicinity [21]. In figure 2.7 substitutional and interstitial foreign atoms defects and vacancy are described.

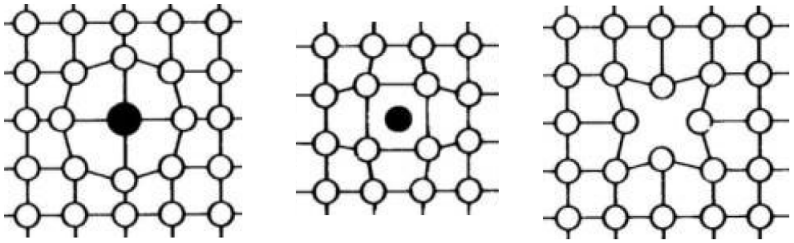

Figure 2.7: *From left to right: Substitutional foreign atom defect, interstitial foreign atom defect and vacancy defect [21].*

Looking at figure 2.7 it can be seen that a vacancy defect is created when a site normally occupied by atoms is left empty. Foreign atoms, also called impurities, can be included in the crystal lattice, during production of the material or afterwards by diffusion, and occupy different sites. When impurity atoms fill in the voids between host atoms they are referred as interstitial impurities, while if they replace a host atom, they are referred as substitutional impurities. This notation will be used frequently in the next sections of the thesis.

Grain Boundaries

A grain boundary is a two dimensional defect, defined as the boundary separating two small grains or crystals having different crystallographic orientations in multicrystalline materials [45]. A schematic representation of a grain boundary is shown in figure 2.8.

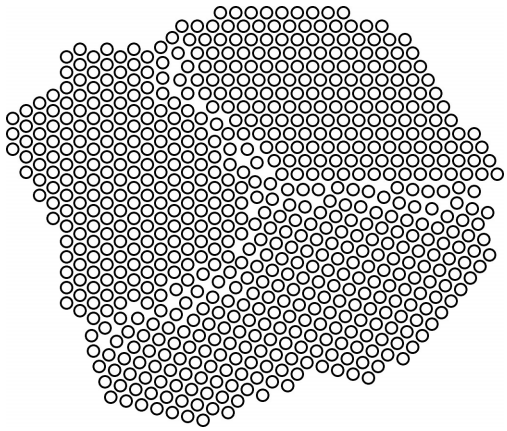

Figure 2.8: *Schematic representation of a grain boundary.*

An important characteristic of the grain boundaries is that the atoms are less regularly bounded and possess a higher chemical reactivity. Therefore impurity segregation is more likely to occur along the boundaries [21].

2.3 Solidification

Solidification theory is of fundamental importance in order to understand the solute concentration, the structure and the related properties of the material under examination. Moreover SiGe, as an alloy, requires an accurate study of the phase diagram and segregation dynamics. This chapter will briefly explain basic concepts regarding solidification and crystal growth which are relevant for SiGe alloy.

2.3.1 SiGe Phase Diagram

The mechanical properties of an alloy are strictly related to its microstructure, which is connected with the characteristic of its phase diagram. A good understanding of the phase diagram is necessary to bridge between macroscale and microscale features. *Phase diagrams* are often named as equilibrium diagrams since they show the phases in equilibrium with each other at various temperatures plotted against pressure or composition. A *phase* can be defined as a homogeneous portion of a system that has uniform physical and chemical characteristics [22]. If more than one phase is present they will have different physical and/or chemical properties and a boundary will separate one from the other.

In a two component system, as SiGe alloy, a binary phase diagram is used. It is a map that represents the relationships between temperature, compositions and quantities of phases at equilibrium, which influence the microstructure of an alloy [22]. In this case pressure is kept constant at 1 atm.

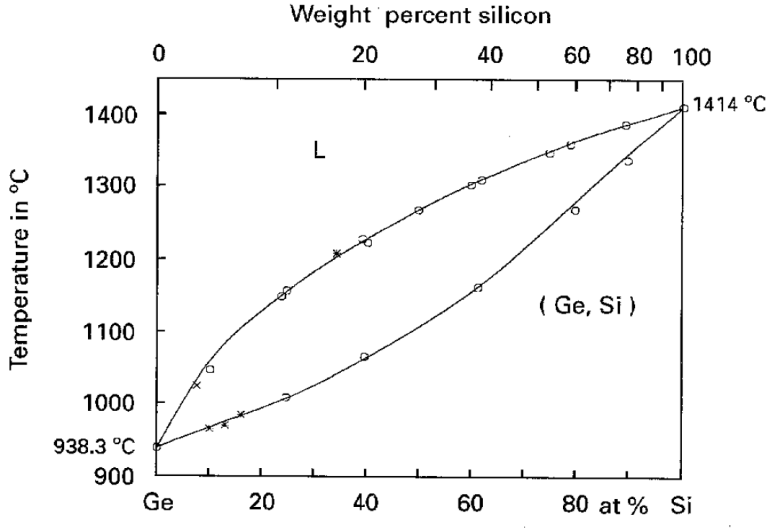

Figure 2.9: *SiGe assessed equilibrium phase diagram. [60]*

The phase diagram of SiGe alloy, studied in this project, is taken as example. In figure 2.9 it is possible to distinguish three areas. In the top left hand corner L

is a homogeneous liquid solution of both Si and Ge. In the lower right hand corner region the two components of the alloy are perfectly miscible in the solid state. The region between the two lines is called the two phase region, in which both solid and liquid phase are present. This kind of system is known as *isomorphus* since the two components of the alloy are completely soluble in each other. The complete solubility can be explained by the fact that silicon and germanium have the same crystal structure, similar electronegativity and valences. Due to this characteristic both the components can be identified as solute, if they are present in lower percentage compare to the other.

The lines dividing the two phase zone are called *liquidus* and *solidus*, the first is next to the liquid area while the second is next to the solid area. Those lines intersects the composition extremes identifying the melting points of Si at 1414°C and Ge at 938°C. Hence, for each composition with both components involved the melting happen in the gap between solid and liquid phase in a two phase regime. To calculate the phase composition in this area it is necessary to introduce the *tie line*, which is an horizontal line that extend from a phase boundary to the other, see figure 2.10. Given a specific temperature the intersection of the tie line with the liquidus line will give the liquid phase composition C_L while the intersection with the solidus line will give the solid phase composition C_α, as in figure 2.10.

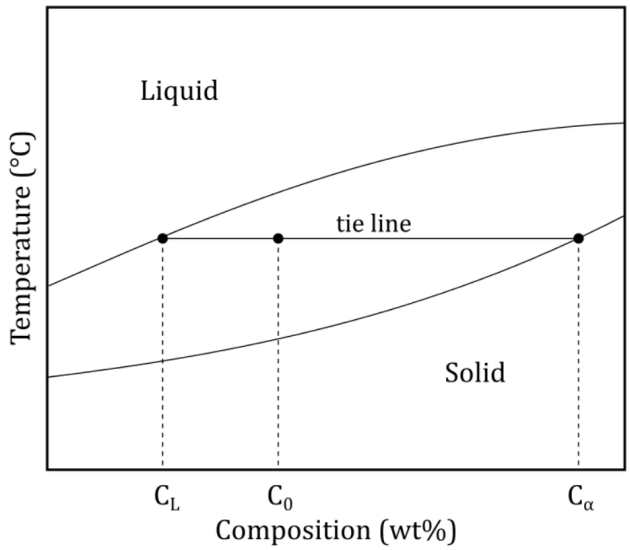

Figure 2.10: *Phase diagram showing a tie line and the relative composition C_L and C_α of the components in the two phase region at a certain temperature.*

2.3.2 Crystal Growth and Segregation

Crystal growth is the basic process in melts solidification for all cast materials, it is controlled by the heat and mass transport and determines the quality of the product (grain size, micro segregation, structure ect). The phase separation derived from the

SiGe phase diagram in figure 2.9 leads to the definition of the *equilibrium partition ratio* k_0:

$$k_0 = \frac{C_s}{C_L} \tag{2.5}$$

where C_s is the concentration of solute in the solid, and C_L the concentration in the liquid. In the system under investigation the large separation of the liquidus and solidus line will give rise to a difference in composition between solid and liquid phase during solidification which is then described by the parameter k_0.

Considering an initial liquid concentration C_0, the composition of the first solid will be $k_0 C_0$. Afterwards if $k_0 < 1$ during solidification, the liquid next to the solidification interphase will experience a solute diffusion from the solid phase. According to Tiller et al. [23], under limited diffusion in the liquid the solute is transported away from the interphase and the melt composition is not becoming instantly homogeneous. An initial transient is then established until the concentration in the solid approaches C_0 and a steady state is reached, see figure 2.11. Considering a molten of binary alloy, it is in stationary conditions when it has:

- planar solidification front
- constant growth rate
- negligible diffusion rate in the solid phase compared to the liquid
- no convection in the melt
- constant values of k
- composition of the melt in the bulk equal to the composition of the solid

The *steady state* condition is defined when the number of solute atoms rejected from the solid per unit time is equal to the number of solute atoms which leave the interface per unit time by diffusion into the melt. The concentration of solute in the liquid can be calculated as:

$$C_L = C_0 \left(1 + \frac{1 - k_0}{k_0} e^{\left(-\frac{v\,x}{D_L} \right)} \right) \tag{2.6}$$

where v is the solidification velocity, x is the distance from the interphase and D_L is the diffusion coefficient of the solute in the liquid.

Equation 2.6 does not apply in the transient time interval, for this reason Tiller at al. [23] developed the equation:

$$C_L = C_0 \left[(1 - k_0) \left(1 - e^{\left(-\frac{k_0\,v\,x}{D_L} \right)} \right) + k_0 \right] \tag{2.7}$$

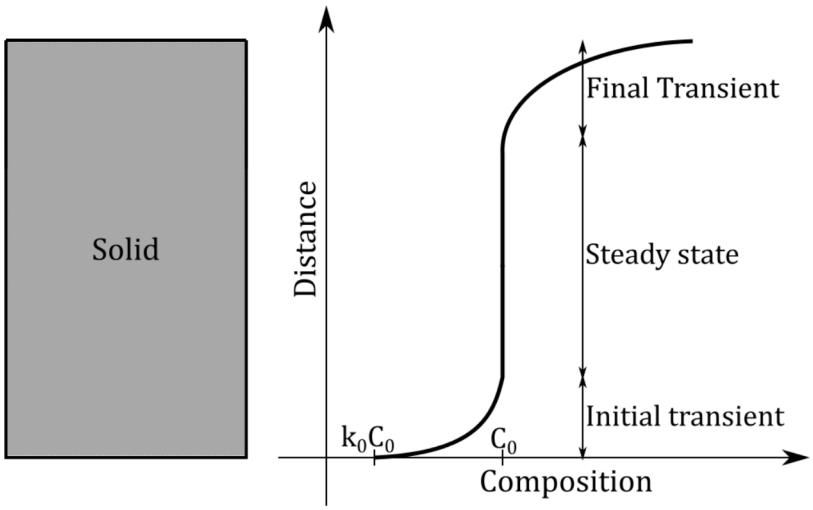

Figure 2.11: *Concentration of solute in an ingot obtained with directional solidification under Sheil hypothesis (i.e. no solid diffusion and limited diffusion in the liquid). Initial and final transients are magnified for illustrative purpose.*

Function 2.7 is an approximation made not considering convection in the melt and more accurate results have been found by W.W. Mullins and R.F. Sekerka [24] using a more complicated theory, but for most purposes the formula above is sufficient.

Steady state is maintained during directional solidification as far as there is enough liquid and solute to ensure the mass balance. When this requirement is not fulfilled anymore, at the end of the process another transient takes place. The rejected solute is confined at the edge of the rod with increasing gradient, as can be seen in figure 2.11.

Convection

In the model above no convection in the melt has been assumed. A compromise between Tiller et al. and W.W. Mullins theories can be found in a third description, which includes an artificial separation of the diffusion process and the convection process. The separation is made introducing a layer of width δ_d where no convection is present and in which the Tiller distribution can be assumed. After this small region, due to convection, the solute is mixed uniformly and the melt will have a constant composition.

where

$$\delta_d = \frac{2\,D_L}{v} \tag{2.8}$$

the value δ_d is strictly related to the convection influence: the higher the convection the smaller will be the width of this separation layer.

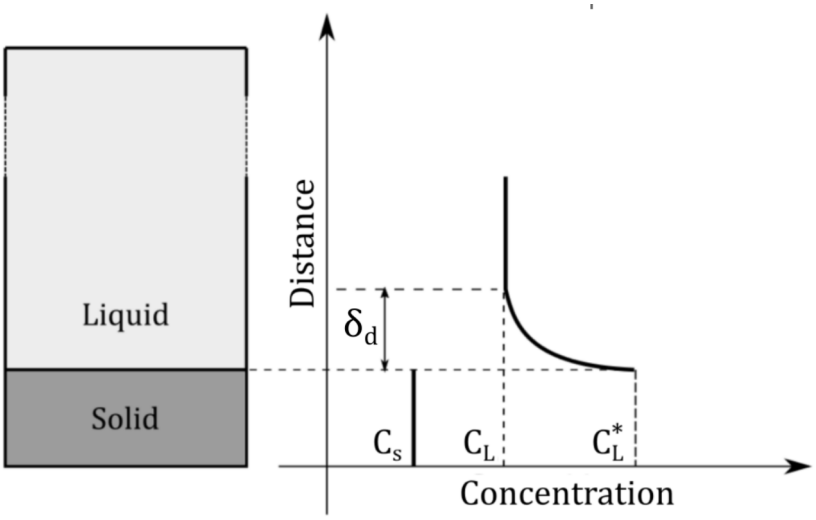

Figure 2.12: *Concentration of solute in a solid liquid interface. The model considers convection in the melt and a layer δ_d separating the phases.*

Furthermore in this model the concentration of solute at the interphase is changed, as can be seen in figure 2.12. C_S^* and C_L^* are lower compared to the concentration values in the system with no convection, while C_0 now is higher because the melt is homogeneously mixed. All these changes require a new *effective partition coefficient* k_{eff} defined as the ratio of the final solute concentration in the solid to the average solute concentration in the melt [25] :

$$k_{eff} = \frac{C_S^*}{C_L} \tag{2.9}$$

where C_L in this case is the average solute concentration in the liquid phase, as it is also in figure 2.12. Burton, Prim and Slichter in their work [26] found the function for k_{eff} to be:

$$k_{eff} = \frac{k_0}{k_0 + (1 + k_0)e^{-\frac{v\,\delta_d}{D_L}}} \tag{2.10}$$

Finally Scheil's equation can be introduced:

$$C_S = k_{eff} C_0 (1 - f)^{(k_{eff} - 1)} \tag{2.11}$$

where f is the solidified fraction of the rod. Equation 2.11 describes how the solute concentration varies along the rod and it is often used to calculate segregation.

Metallic Impurities

During directional solidification not only germanium but all the impurities present in the silicon melt are following the behavior just described above. The properties

of mc silicon like minority carrier lifetime or diffusion length, which are important properties for solar cells efficiency, are correlated to the content and the occurrence of C, N, O, metals and unintended dopants [27].

Impurity	**Equilibrium partition ratio** k_0
Fe	$8.0 \cdot 10^{-6}$
Ti	$3.6 \cdot 10^{-4}$
Al	$2.0 \cdot 10^{-3}$
Cu	$4.0 \cdot 10^{-4}$
Ni	$8.0 \cdot 10^{-6}$
B	0.8
P	0.35
O	0.25-1.25
C	0.07
Ge	0.45

Table 2.1: *Equilibrium partition ratio of selected impurities in silicon [28] [29]. The value of Ge is taken from [30]*

In table 2.1 a list of impurities and related k_0 values is presented. Metallic impurities have values noticeable lower than all the others, which implies a steeper final transient according to Scheil's equation 2.11. Therefore directional solidification is an effective process to refine silicon from metallic impurities which are confined at the top of the ingot. Many of these elements that segregate to the surface, can still dissolve in solid silicon at high temperature, giving rise to the *back diffusion* [31]; this reduces the properties of the region beneath the ingot top surface.

Substitutional Carbon and Interstitial Oxygen

Oxygen and carbon are two major impurities in silicon ingots and are introduced in the material during the crystallization process. Figure 2.13 describes how these impurities are added to the melt.

Looking at figure 2.13, oxygen is included by reaction of the silica crucible with the molten silicon, O and Si react forming SiO(g) which evaporates from the melt. Carbon impurities are added when the evaporated SiO gas reacts with the graphite heater or other carbon-containing parts in the furnace [32]. These two elements, when the crystal is finally solidified, create defects in the lattice structure, influencing the material properties. Oxygen can occupy interstitial sites between silicon atoms or form SiO_2 precipitates, in both cases it is related to lattice dilatation and internal stresses [33]. SiO defects can be electrically active and behave as donor elements called Thermal Donors. They are double donors generated in the temperature range 400–500°C and annihilated at temperatures above 650°C [34]. Carbon

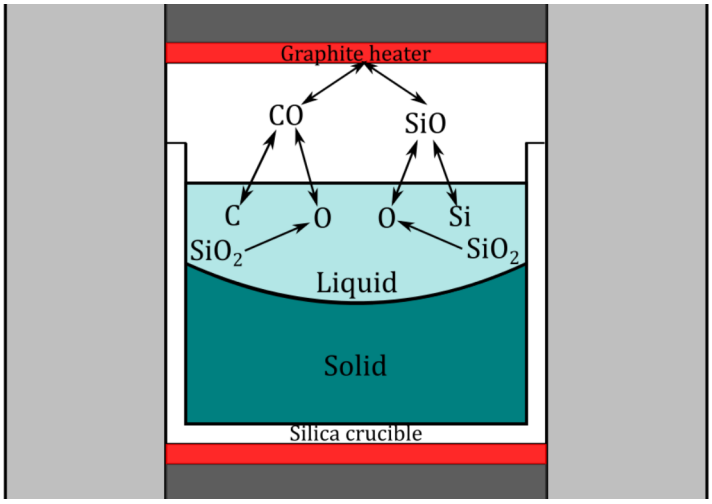

Figure 2.13: *Carbon and oxygen cycle during silicon crystallization.*

instead occupies substitutional sites or form SiC precipitates; it is not electrically active, but can facilitate oxygen inclusion and reduce the mechanical properties [27]. Therefore both substitutional carbon (C_s) and interstitial oxygen (O_i) are undesired defects that have been characterized in this thesis.

Interface Stability

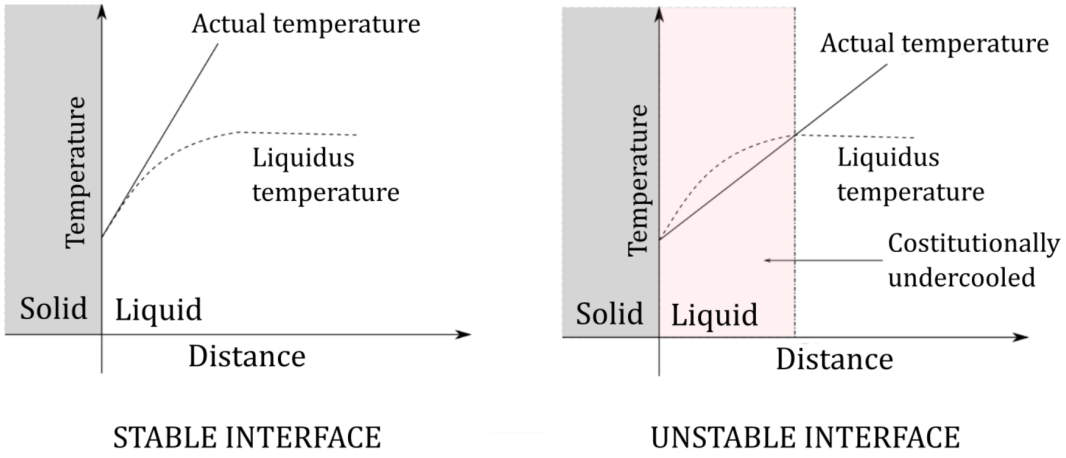

Figure 2.14: *Equilibrium and real temperature distribution along the melt of a binary alloy [25].*

The interface is defined stable if, when it is disturbed, it returns spontaneously to its initial state. If it does not happen then the interface is unstable. Considering a planar interface during the solidification of an alloy's melt, the temperature distribution as a function of distance is controlling the stability of the process [25]. It is

possible to derive the equilibrium temperature distribution by combining the phase diagram, figure 2.9, and the solute concentration equation 2.6. It is also reasonable to consider that solid and liquid phase are in thermal equilibrium at the interface, while elsewhere the temperature of the melt will differ from the equilibrium, as can be seen in figure 2.14.

The interface will return spontaneously to its initial state if the perturbation is absorbed after it. A perturbation, in this case, can be an undercooling of the solidification front, which will be dissolved if the temperature gradient is positive. Nevertheless this requirement is necessary but not sufficient to keep a stable interface. As a matter of fact, the crucial feature for what concerns interface stability is the gradient of the actual temperature compared with the equilibrium temperature distribution, also called liquidus temperature, see figure 2.14. If the gradient of the actual temperature is lower than the one of the liquidus temperature, the perturbation will grow. This phenomenon is called *constitutional undercooling* and can be avoided applying high temperature gradients at the solidification interface or slow growth rates.

2.3.3 Directional Solidification

Directional solidification is a process used to cast multi crystalline silicon (mc-Si) in a crucible. It is a simpler process compared to the Czochralski (CZ) method, used to produce mono crystalline silicon, and therefore can reduce the production costs and increase the productivity of Si for solar cells. Moreover the mc-Si ingots are not cylindrical and they can be cut in rectangular shapes without a big waste of refined silicon. The drawback is that the material produced has a lower quality, mainly due to grain boundaries and dislocations which consequently reduce the energy conversion efficiency. In this perspective the ideal solution would be to improve the material quality of without increasing complexity and costs of the production process. The inclusion of a small Ge percentage, studied in this project, is one of the possible alternatives.

During directional solidification, the silicon feedstock is placed in a SiO_2 crucible coated with Si_3N_4 to prevent Si to stick on the crucible. The temperature is raised until the material is melted and then a vertical temperature gradient is established. Solidification is directional from the bottom to the top of the crucible with a near planar solidification interface [35]. To achieve this result there are two main methods and hence two furnace types. The first one is called the Bridgman method, in which the thermal gradient is created using a moving stage to vertically translate the crucible while the heaters are fixed. The second method is the Vertical Gradient Freeze (VGF), in this case the crucible is immobile and the gradient is established removing the heat from the bottom using a heat exchanger. The latter was used to produce the ingots analyzed in this thesis and it will be further discussed in chapter 3.

2.3.4 Zone Refining

Zone refining is a popular type of recrystallization technique used mostly in the electronic industry to enhance the purity of semiconductor's crystals. Recrystallization processes nucleate new grains from an already grown crystal or amorphous region in a controlled manner [36].

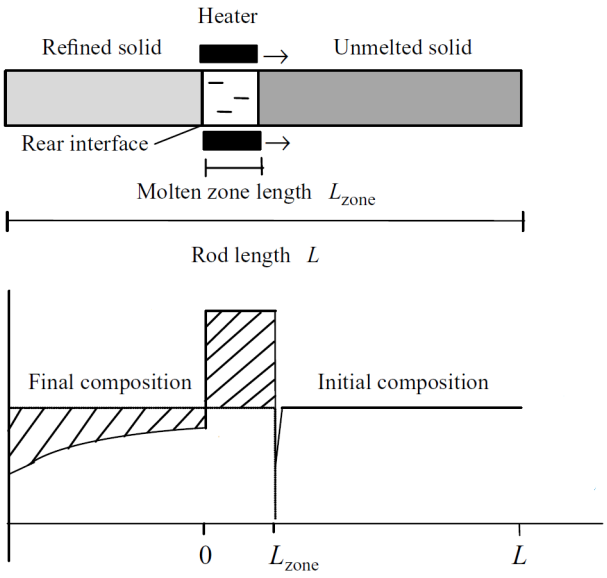

Figure 2.15: *Sketch of a zone refining equipment and of the solute distribution in the rod in case of complete mixing in the molten zone. The marked areas in the figure are suppose to be equal [25].*

Particularly, in the technique used to anneal part of the examined microwires, a molten zone is created and translated through the rod. It can be melted using a concentrated heat source or a solvent and heat. During the translation the solid is melted in the front plane while it solidifies behind it, see figure 2.15. Due to the concentration difference, explained in the previous sections, the impurities are confined in the final transient. Furthermore, controlling the solidification rate, it is also possible to improve the quality of the crystal structure, avoiding perturbations during the process.

In this study case the SiGe wires were recrystallized using a CO_2 laser. This method creates a substantially high temperature gradient which is of great value for stability in solidification and can also allow to high growth velocity. The molten zone will be Ge rich and give rise to an initial and a final transient, with a steady-state region in between.

2.4 Characterization Techniques

The main characterization techniques used in the thesis are described in this section in order to understand the components of the instruments used and the fundamental physics behind them.

2.4.1 Glow Discharge Mass Spectrometry (GDMS)

Glow Discharge Mass Spectrometry (GDMS) is a technique used to measure the chemical composition of semiconducting and conducting samples. Its main elements are shown in figure 2.16.

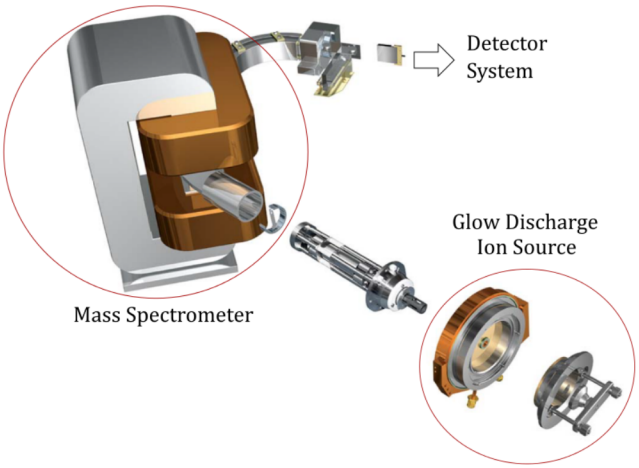

Figure 2.16: *Main components of the Glow Discharge Mass Spectrometer. Modified from [37].*

The GDMS instrument is based on three components: ion source, mass spectrometer and detector system. First of all an inert gas, in this case Ar, flows at reduced pressure towards the sample. A voltage between the sample (cathode) and the anode charges positively the gas atoms in the cell creating a glow discharge. The argon ions accelerate and impact on the sample surface sputtering away atoms. Due to charge transfer, penning ionization and electron ionization, the sputtered atoms become positively charged and are extracted from the low pressure cell to the mass analyzer. The mass spectrometer uses a magnetic field, set by a magnet in the instrument, to separate the sputtered ions according to equation:

$$r = \frac{mv}{qB} \tag{2.12}$$

where r is the radius of the deflected ions trajectory, B the magnetic field and m v and q are the ion mass ,velocity and electric charge. Given that v and B are constant values in the system, r is then a function of the mass to charge ratio m/q. The detector finally adjusts the aperture at different angles to select particular m/q ratio and count the ions of the chosen impurity isotope.

GDMS has a low detection limit, in the order of tenths of ppb, and therefore is commonly used for the analysis of impurity elements in silicon for solar applications. It can also calculate the concentration of several isotopes in the same analysis reducing the time required for the experiments. A major drawback is that it is a destructive technique, the sample bombarded with ions loses several atom layers each time is analyzed, for a thin sample this can be a big limitation. Furthermore the analyzed spot has a quite large diameter, $22mm \leq \varnothing \leq 70mm$, reducing the resolution and making the instrument not suited for local analysis of the composition.

2.4.2 Fourier Transform Infrared Spectroscopy (FTIR)

Fourier Transform Infrared Spectroscopy (FTIR) is a technique in which the absorption or transmission spectra, created using infrared (IR) radiation passing through solid, liquid or gas samples are studied to analyze the sample chemical composition. The IR radiation is emitted by a black-body source and directed to the interferometer, the black box in figure 2.17.

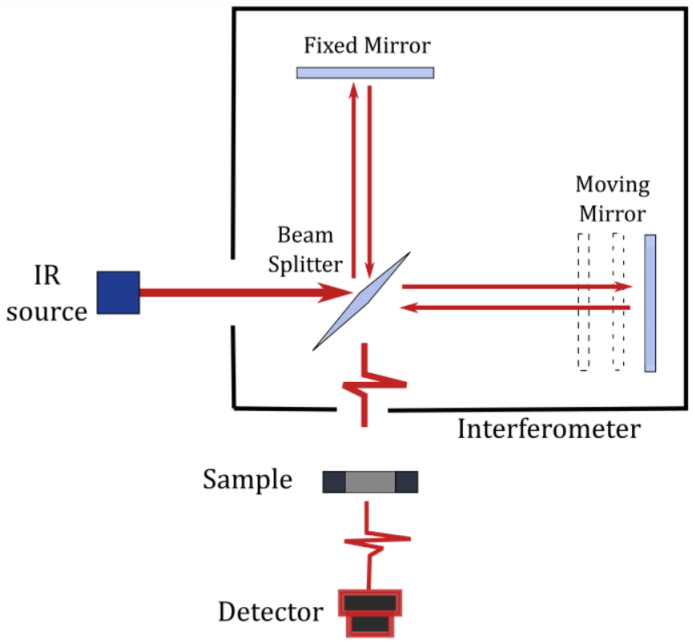

Figure 2.17: *Main components of the FTIR instrument in a simplified description.*

The interferometer is the core of FTIR. It is composed of a beam splitter which takes the incoming infrared beam and divides it into two beams with different directions. One beam is directed to a fixed mirror while the other is directed to a moving mirror. After being reflected the beams then recombine at the beamsplitter. Since they traveled different paths they will interfere with each other creating the interferogram, which is the output signal of the interferometer [61]. In this signal is encoded every IR frequency information as a function of the moving mirror distance.

The signal passes through the sample and is then collected by the detector. At this point the signal contains all the frequency simultaneously and needs to be decoded by a computer using the Fourier Transform; the transmission or absorption spectrum is then saved. Finally a background spectrum, previously collected without any sample in the instrument, is subtracted to the test spectrum by the software, leaving only the sample contribution. The resulting spectrum is a unique description of the sample molecular bonding, since a precise set of energy/frequency of the IR radiation has been absorbed. Analyzing the absorption peaks it is possible to determine the composition of the sample and quantitative methods can be developed and calibrated.

2.4.3 Four Point Probes (FPP)

The four point probes (FPP) is a method used to measure the resistivity (ρ) of materials, the set-up is described in figure 2.18.

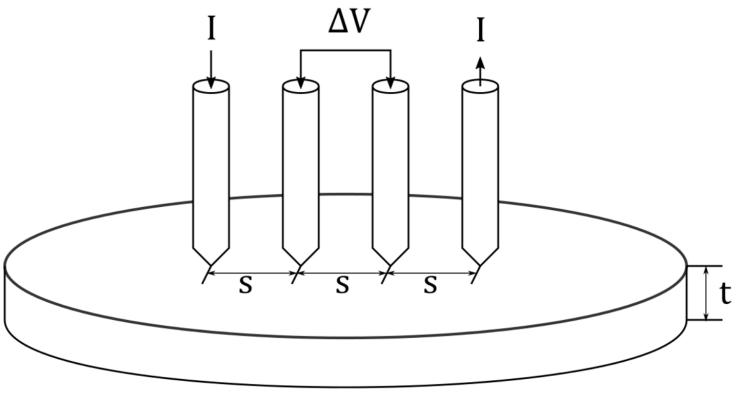

Figure 2.18: *Four point probe measurement setup.*

The measurements are done using four probes aligned and in contact with the material surface, then a current is passed trough the two outer probes while the voltage between the inner one is measured. From the known value of current (I) and the measured voltage (ΔV) it is possible to calculate the resistance.

$$R = \rho \left(\frac{dx}{A} \right) \tag{2.13}$$

where dx is the radius of the region in which the current is going to distribute and A is the area of the sample. If we consider the area to be A=2πxt with t the sample thickness, as in figure 2.18, then the resistance becomes:

$$R = \int_{s}^{2s} \rho \left(\frac{dx}{2\pi x t} \right) = \frac{\rho}{2\pi t} ln(2) \tag{2.14}$$

in this particular situation 2R = (V/I) and therefore we can deduce ρ to be:

$$\rho = \frac{\pi}{ln(2)} \frac{V}{I} t \tag{2.15}$$

Equation 2.15 is correct if the probes are placed at a distance d>2s, with s the spacing between the probes, and t≫s. If the last constraint is not fulfilled a correction coefficient $F\left(\frac{t}{s}\right)$ will have to be applied [39].

2.4.4 Optical Measurements

In this work a simplified analysis of the interaction between the electromagnetic radiation and the samples material is adopted. The simplification holds on the assumption that the wavelength of the radiation is much smaller than the scale of material boundaries and wave-optical effects (diffraction) can be neglected [40]. The second assumption is expressed in the equation:

$$Abs = 1 - Ref - Tr \tag{2.16}$$

where Abs, Ref and Tr are the fractional sample absorption, reflection and transmission. Several experimental methods can be used in order to measure these values but they can generally be divided in two main categories according to the sample surface. If the surface can be assumed to be perfectly flat, *specular surface*, then the angle of reflection equals the angle of incidence, and the qualities of the outgoing reflected beam are the same as the incident one. In this case a simple detector positioned in the direction of the transmitted or reflected light can be used. Most likely, instead, the surface will have a roughness component and reflect light in a range of solid angles, requiring a more complicated detection system. A spectrophotometer in transmittance mode was used in this thesis for samples double side polished (DSP), hence considered having a specular surface, while an integrating sphere has been utilized for the second kind of samples. These two techniques are described below.

Spectrophotometer

A spectrophotometer is used to measure transmittance or reflectance of samples within a range of wavelength described by a combination of a light source and monochromator. A simplified description of the spectrophotometer components is shown in figure 2.19.

In transmission mode, light from the source is passed through a monochromator, the function of which is to produce a beam of monochromatic (single wavelength) radiation that can be selected from a wide range of wavelengths. Its main component is a dispersive element, such as a prism, which separates the spectral components in angle space; the angular deflection of a plane wave is in fact wavelength dependent [41]. After dispersion the spectrum is focused at the exit slit which may be scanned

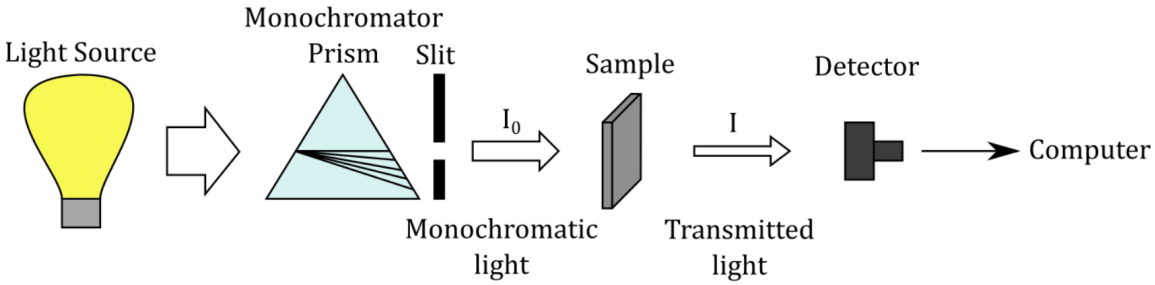

Figure 2.19: *Simplified description of the spectrophotometer components. The image refers to a transmission measurement.*

across the beam to isolate the required wavelength. In practice the prism is normally rotated to cause the spectrum to move across the exit slit. The monochromatic light is then passed though the specular sample and the transmitted component is measured by the detector.

Integrating Sphere

The integrating sphere is a device used to measure optical radiation for samples in which no angular dependence of the reflectance profile is desired. To understand the device applications it is necessary to analyze how a flux of light behaves in the sphere and to describe some fundamental parameters. First of all the *radiance* is defined as the flux density per unit solid angle and can be used to predict the amount of flux that can be collected by an optical system that might view the illuminated surface [42]. The radiance, L, of a diffuse surface for an input flux Φ_i can be expressed as:

$$L = \frac{\Phi_i \, \rho}{\pi \, A} \tag{2.17}$$

where ρ is the surface reflectance, A the illuminated area and π the total projected solid angle from the surface.

In an integrating sphere the radiance should take into account multiple surface reflections and losses through port openings. The port fraction term, f_p, is then defined as the sum of the ports area divided by the sphere area and the amount of flux reflected on the entire sphere is $\Phi_i\rho(1-f_p)$. This flux is then reflected again giving $\Phi_i\rho^2(1-f_p)^2$, hence after n reflection the flux will be equal to

$$\Phi_{tot} = \Phi_i\rho(1-f_p)\left\{1+\rho(1-f_p)+...+\rho^{n-1}(1-f_p)^{n-1}\right\} \tag{2.18}$$

which expanded to an infinite number series gives:

$$\Phi_{tot} = \frac{\Phi_i\rho(1-f_p)}{1-\rho(1-f_p)} \tag{2.19}$$

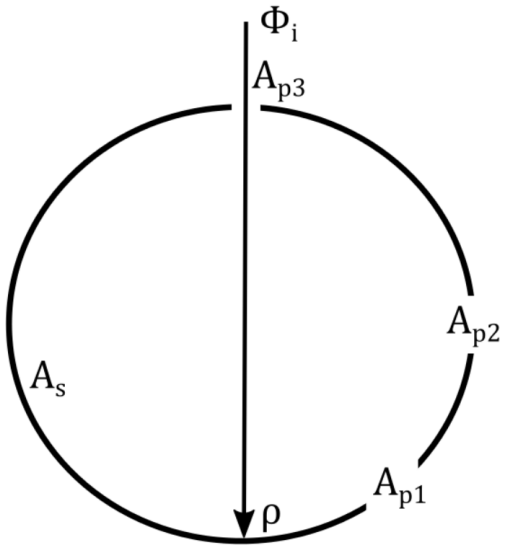

Figure 2.20: *Schematic of an integrating sphere with an incoming light flux* Φ_i*, wall reflectance* ρ*, sphere area* A_s *and three ports of area* A_{p1}*,* A_{p2} *and* A_{p3}*.*

this last equation shows that the total flux is higher than the input flux due to the multiple reflections. The increase in radiance can be accounted by the parameter called *sphere multiplier*

$$M = \frac{\rho(1-f_p)}{1-\rho(1-f_p)} \tag{2.20}$$

which is strongly dependent on the sphere reflectance and opening ports area. In the present work the integrating sphere device has been used for reflectance measurements using the substitutional method approach. It compares the wall flux due to irradiation of the test sample with the flux of a sample having a known reflectance. The measured flux will be equal to $\Phi_i \rho_s M_s$ for the sample and $\Phi_i \rho_r M_r$, hence the ratio of the two measurements will be:

$$\frac{\Phi_s}{\Phi_r} = \frac{\rho_s M_s}{\rho_r M_r} \tag{2.21}$$

finally given that M_s=M_r the sample reflectance is measured as:

$$\rho_s = \rho_r \frac{\Phi_s}{\Phi_r} \tag{2.22}$$

2.4.5 Scanning Electron Microscope (SEM)

A scanning electron microscope (SEM) is a type of electron microscope which uses a beam of electrons to scan the surface of the sample and acquire images. The usual components of an SEM are described in figure 2.21.

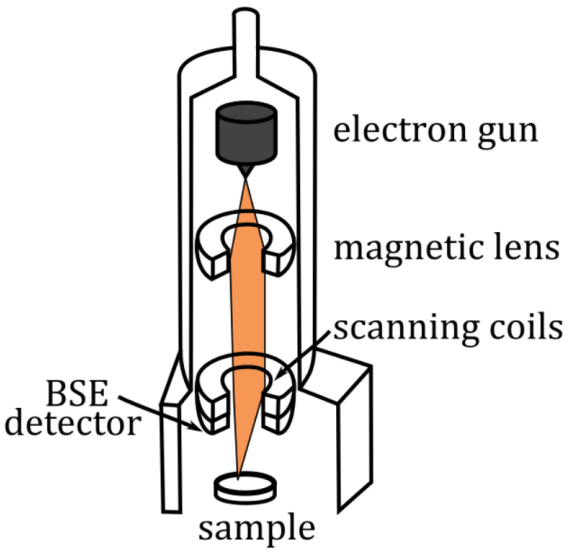

Figure 2.21: *Schematic of a scanning electron microscope (SEM) components.*

The electron beam is generated by the electron source, usually a Tungsten filament heated to about 2700 K. At that temperature the electrons have enough thermal energy to be extracted by an electric field and accelerated to an energy between 1 and 30 keV. The divergent electron beam is then focused on the sample using a series of electromagnetic lenses and scanned on the surface by control of the current in the scanning coils. The electrons, interacting with the sample's atoms, dissipate energy and generate various secondary emissions that are finally collected by the detectors system [43]. There are several types of detectors and each of them is collecting the result of a particular interaction between the sample and the specimen, therefore providing different information about the specimen. In this thesis the SEM has been used only to collect images trough back scattered electron (BSE) detection. The BSE are defined as electrons that have lost a small portion of their initial energy. This type of scattering is caused by the interaction of the incoming electrons with the electrostatic potential of both the core and the electrons of the atoms in the specimen. The amount of elastic scattering is strongly affected by the atomic number (Z), and increases approximately as Z^2 [43]. Therefore a BSE image can, if the Z variation is high enough, give compositional contrast. This type of contrast is weak compared to topographic contrast and the sample needs to be polished flat to gain reliable compositional information.

3

Experimental Methods

This chapter will first explain the casting method of the ingots, the cutting procedure and the wafers nomenclature. Then a description of the microwires production process and their sample assembly is carried out followed by the experimental setups and calculations.

3.1 Casting Method

The casting process has been carried out using the VGF technique explained in section 2.3.3. For this thesis a VGF furnace in the Materials Science department of NTNU has been used, the main components are described in figure 3.1.

The furnace in figure 3.1 is made of a crucible containing the melt, one top and bottom heaters at temperature T_1 and T_2, insulating walls surrounding the crucible and finally a heat exchanger cooled by water, placed beneath the bottom heater [35].

The 1 kg ingots are both positively doped with B (∼0.17g), giving a dopant density of $1.5 \cdot 10^{16}$ cm^{-3}. In the SiGe alloy ingot 1% of Ge 99.999% pure is added (∼10.17g). The crucible is made of silica and Si_3N_4 is sprayed on the inner surface to prevent sticking of the silicon melt. After been filled with the raw materials, the crucible is placed between the two heaters. These components are resistive elements made of graphite. A molybdenum plate is used between the bottom heater and the crucible to homogenize heat. A control interface, built using LabVIEW, monitors the temperatures T_1 and T_2, measured by tungsten/rhenium thermocouples, and consequently adjusts the power inputs of the heaters in order to follow the temperature setpoints initially decided. The temperature setpoints used in this thesis are described in figure 3.2.

During solidification the presence of oxygen in contact with high temperature graphite elements generates CO(g) [35], which can dissolve on the melt surface and pollute the ingot. The chamber is therefore pumped to vacuum levels of 10^{-4} mbar or lower using an oil-sealed rotary vane pump assisted by a secondary turbo molecular pump. Once the vacuum is established, the chamber is quickly filled with argon through a molybdenum tube until a pressure slightly higher than atmospheric is

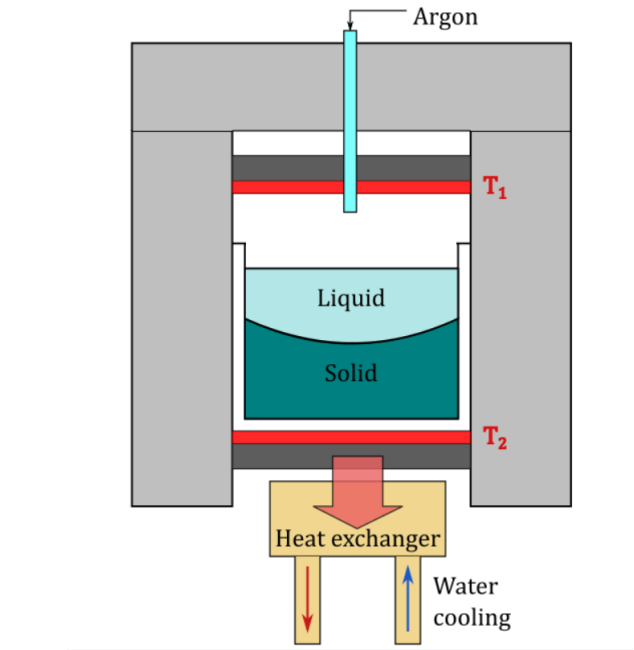

Figure 3.1: *Vertical Gradient Freeze (VGF) furnace sketch. The temperatures T_1 and T_2 can be adjusted to create different vertical gradients. The grey sections are the insulating walls.*

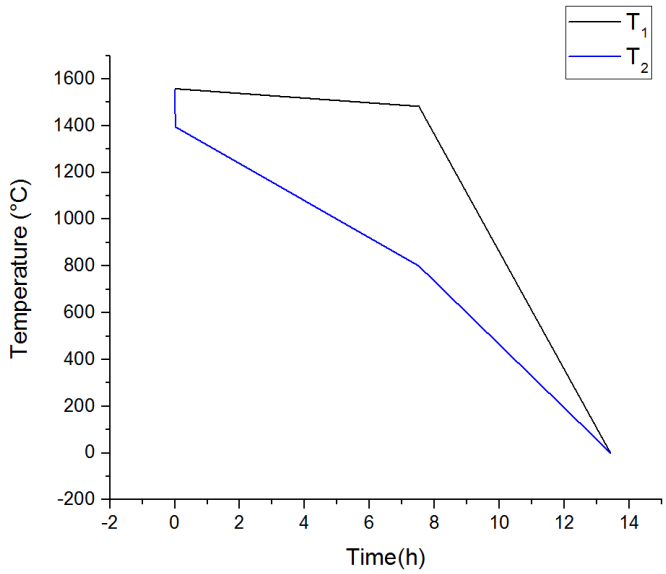

Figure 3.2: *Temperature vs time graph of the cooling process. T_1 and T_2 are the setpoints followed by the control interface program.*

reached. Argon is flushed on the melt during all the process to reduce as much as possible CO(g) pollution.

3.2 Samples Preparation and Nomenclature

The two cylindrical ingots, after being crystallized, had a diameter of ∼10cm and height of $\sim 4.5cm$. In order to analyze them, the ingots have been cut in the NTNU Glassblowing Workshop has depicted in figure 3.3.

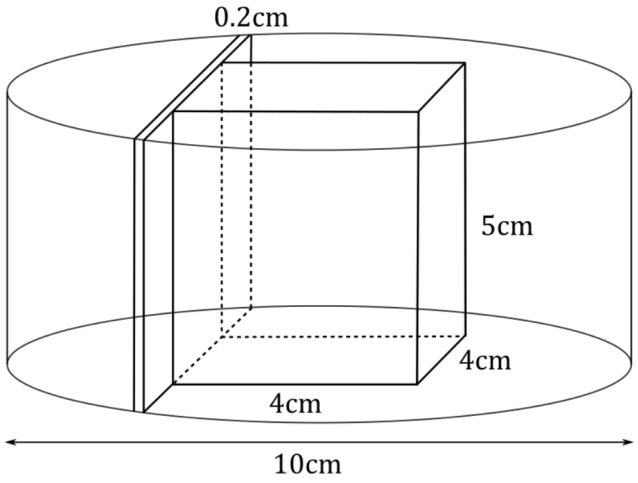

Figure 3.3: *Ingots geometry and sketch for the cutting.*

From the whole ingot were extracted the central $4 \times 4 \times 5$ cm part and a 2 mm vertical slice next to it, cutting the ingot with a diamond blade. The central parts of Si and SiGe ingots were then sent to VARIO Kristallbearbeitung where they have been horizontally cut in 27 wafers each, of which 6 were Double Side Polished (DSP). In Table 3.1 are listed the wafers names and geometrical specifications, for the horizontal cuts the numeration goes from top to bottom.

Due to irreversible damage during the cutting a second larger slice of 3mm SiGe vertical was used instead of the 2mm slice.

In table 3.2 are reported the sample used for the optical measurements in the integrating sphere. The sample ref_opt is a painted glass used as reference for the measurements. Sample SI_3_opt and GE_3_opt were obtained cutting a small piece of SI_3 and GE_3 wafers in order to fit into the integrating sphere. Samples notann_opt, ann_opt and glass_opt need a wider description about their assembly process, which is given in the next section.

3.2.1 SiGe Fibers Production and Assembly

The fibers analyzed in this work are microwires with a core of SiGe alloy and a SiO2 cladding. They have been produced using the molten core fiber drawing technique [44], which is similar to the one used for optical fibers but with a hollow tube. The cylinder was filled with SiGe (6% Ge) and CaOH was used at the interface between the alloy and the SiO_2 layer. The glass was heated up to $\sim$ 2000°C and drawn. SiGe at these temperature, due to its lower melting point, is already molten

Sample Name	Length (cm)	Width (cm)	Height (cm)
Si vertical	0.17	8.80	5.00
SiGe vertical	0.31	8.50	5.00
SI_1	4.00	4.00	0.45
SI_2DSP	4.00	4.00	0.07
SI_3 to SI_13	4.00	4.00	0.10
SI_14DSP	4.00	4.00	0.07
SI_15 to SI_25	4.00	4.00	0.10
SI_26DSP	4.00	4.00	0.06
SI_27	4.00	4.00	0.95
GE_1	4.00	4.00	0.40
GE_2DSP	4.00	4.00	0.07
GE_3 to GE_13	4.00	4.00	0.10
GE_14DSP	4.00	4.00	0.06
GE_15 to GE_25	4.00	4.00	0.10
GE_26DSP	4.00	4.00	0.08
GE_27	4.00	4.00	0.90

Table 3.1: *The table illustrates the samples names and geometrical specifications. Length, Width and Height are oriented as in figure 3.3.*

Sample Name	Length (mm)	Width (mm)	Height (mm)
SI_3_opt	8.60	7.40	1.02
GE_3_opt	8.50	7.00	1.04
notann_opt	3.80	4.20	0.76
ann_opt	3.90	5.00	0.76
glass_opt	3.90	4.60	0.71
ref_opt	8.00	7.00	1.02

Table 3.2: *The table illustrates the samples used in the integrating sphere experiment and their geometrical specifications.*

and it will follow inside the hollow SiO_2 tube. The procedure continued until the desired diameter was reached [36]. At this point a part of the drawn fibers was further treated using a CO_2 laser annealing process to re-crystallize the SiGe core. A schematic representation of these process is shown in figure 3.4.

Both the annealed and as-drawn fibers were cut in smaller segments and horizontally aligned on Polydimethylsiloxane (PDMS) layer. The structure was then fixed with a low-viscosity epoxy (EPO-TEK®301), which is optically transparent across the visible and near infrared regions and has a refractive index similar to silica. The epoxy was cured for 2 hours in an oven at 65°C. Finally the PDMS layer was removed, figure 3.5 shows the horizontal disposition and the different materials

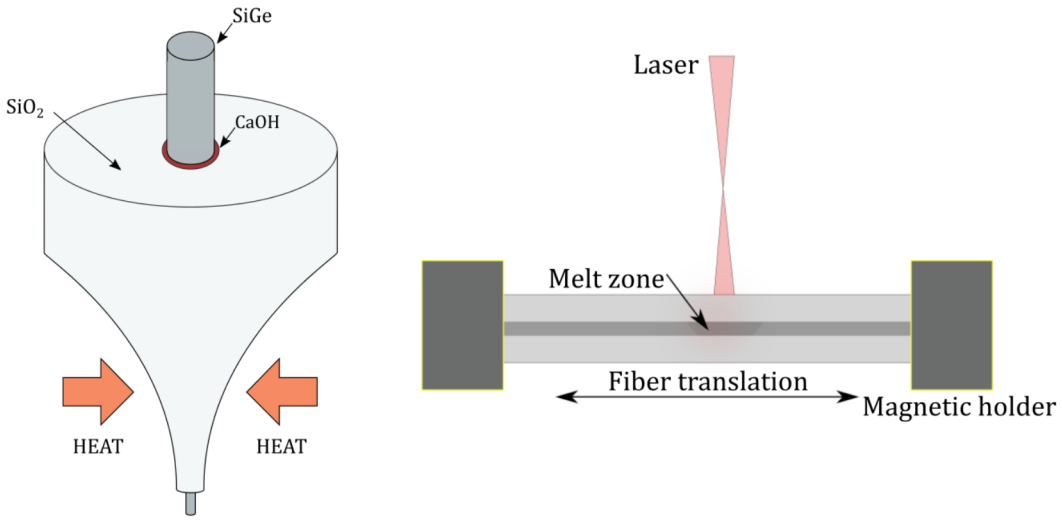

Figure 3.4: *Schematic representation of the production techniques used for the microwires. From left to right, molten core fiber drawing technique and CO_2 laser annealing process [36].*

used.

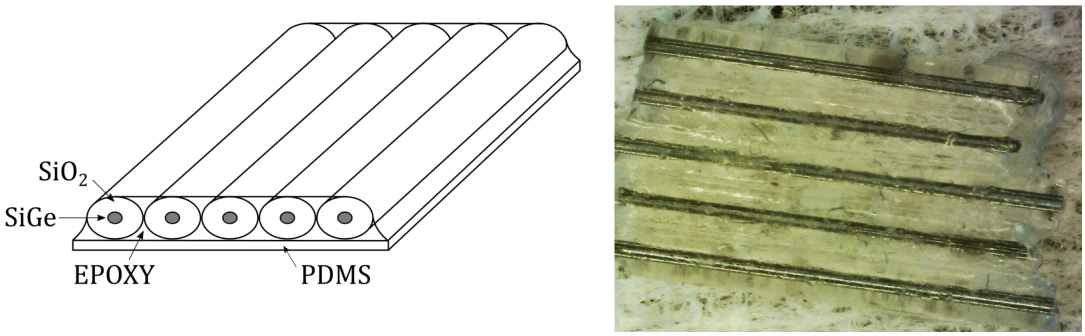

Figure 3.5: *Schematic representation of the horizontal fiber disposition and the materials utilized. PDMS is used as substrate during the sample preparation but it is then removed before the experiments. On the right a picture of notann_opt.*

Referring to table 3.2, ann_opt is the horizontally arranged sample made using the re-crystallized SiGe microwires, notann_opt used the as drawn fibers and glass_opt was made following the same geometrical disposition but using SiO_2 fibers without a semiconductor core.

Fibers for SEM

In order to assess the compositional variations in the SiGe fibers, two segments, one annealed and one not annealed, were analyzed in the SEM tabletop of NTNU

NanoLab. The samples were positioned on a silicon wafer (not part of the investigated ingots), used as flat substrate, in the middle of a plastic ring. Then epoxy was poured to the brim to glue together the fibers and the plastic ring on the silicon substrate. The excess epoxy was removed to get a flat surface, see figure 3.6.

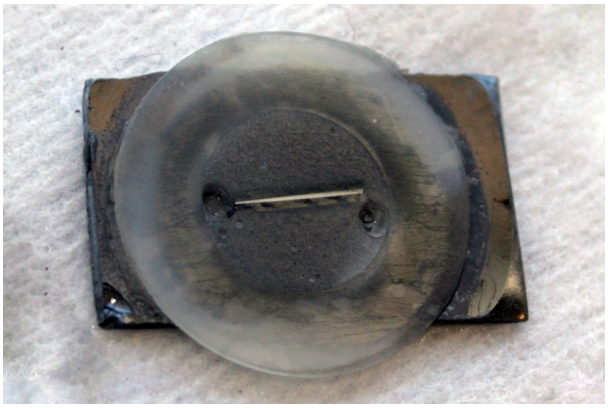

Figure 3.6: *Picture showing one of the samples prepared for the SEM analysis. It can be seen the silicon substrate, the plastic ring and the fiber embedded in epoxy.*

Coarse sandpaper has been used to remove the glass layer and expose the SiGe core, then the semiconductor surface was polished down carefully with the support of a fine grit. The smoothness of the surface was checked all along the process with a light microscope until the desired result was reached. Finally the sample was cleaned prior to characterization with 7 min sonication in iso-propanol and dried with an N_2-gun.

3.3 Resistivity Measurements

The resistivity measurements have been performed at the Department of Physics at NTNU using a Signatone SP4 probe head with 1 mm probe spacing. The Signatone SP4 was then connected to a KEITHLEY series 2400 SourceMeter® which measured the current and voltage signals from the four point probes and communicated it to the computer. The setup is completed by the LabVIEW Software which is used to collect and display IV curves in the range selected by the user before each measurement, an example is shown in figure 3.7.

In this case three horizontally cut samples from both the ingots were analyzed, one from the bottom, one from the center and one from the top. The samples were first placed on the Signatone stage, the four probes were then positioned with particular attention in trying to place them inside the same grain. Crossing grain boundaries can affect the resistivity values [45]. Five or more curves for each sample were collected to better estimate their resistivity. The data has been analyzed with OriginPro 2016 software and a linear fit was applied to calculate the slope of each

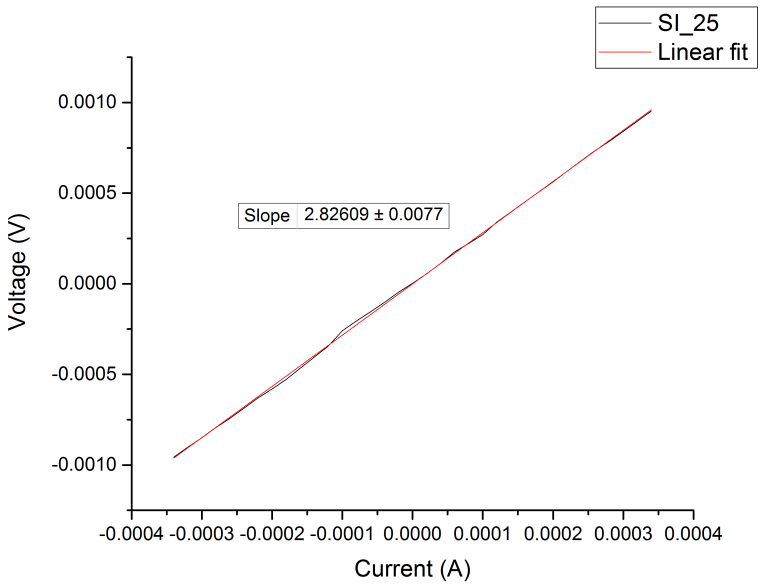

Figure 3.7: *IV curve from the resistivity measurements on sample SI_25. A linear fit (red line) in OriginPro software was used to calculate the slope value.*

IV curve. Recalling the theory of section 2.4.3 the resistivity was finally calculated, since $\frac{t}{s} = 1$ a correction coefficient was applied according with [39].

3.4 FTIR Measurements

FTIR measurements were conducted at the Department of Physics at NTNU using a Bruker Tensor 27 FT-IR spectrometer. The mid-IR source used was an U shaped silicon carbide piece source emitting in the range from 4000 to 400 cm^{-1}. The light was passed through a ROCKSOLID^{TM} interferometer and directed to the sample. The transmitted light was then collected by a DLaTGS detector with integrated preamplifier. The detector converter modifies the analog signal to a digital one, which is sent to the computer and finally processed by the OPUS 6 software. An HeNe laser was used by Tensor 27 to control the position of the moving mirror in the interferometer and hence the data sampling position, as explained in section 2.4.2. For these experiments the two vertical cuts were first Double Side Polished (DSP) at the Department of Materials Science at NTNU using the Abrapol-20 polishing machine. The samples have been examined in five positions with 1 cm spacing, as shown in figure 3.8.

Before each measurement session a background spectrum without sample in the chamber was collected and subtracted from the samples ones. The spectrum for each position was then saved as a text file and further analyzed using OriginPro 2016 software, as described in the next section.

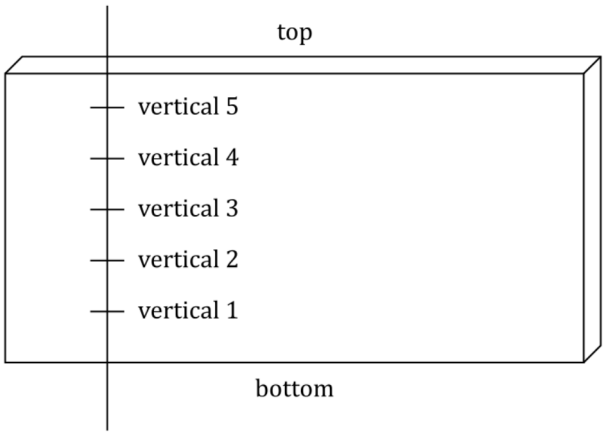

Figure 3.8: *Simplified description of the vertical cuts showing the 5 positions analyzed in the FTIR measurements, the distance between each point is ∼1cm.*

3.4.1 Oxygen and Carbon Concentration Calculations

The FTIR in this study was used in order to identify the interstitial Oxygen (O_i) and substitutional Carbon (C_s) which can be correlated to the absorbance peak in the FTIR spectra at 1107 and 605 cm^{-1} respectively, see figure 3.9.

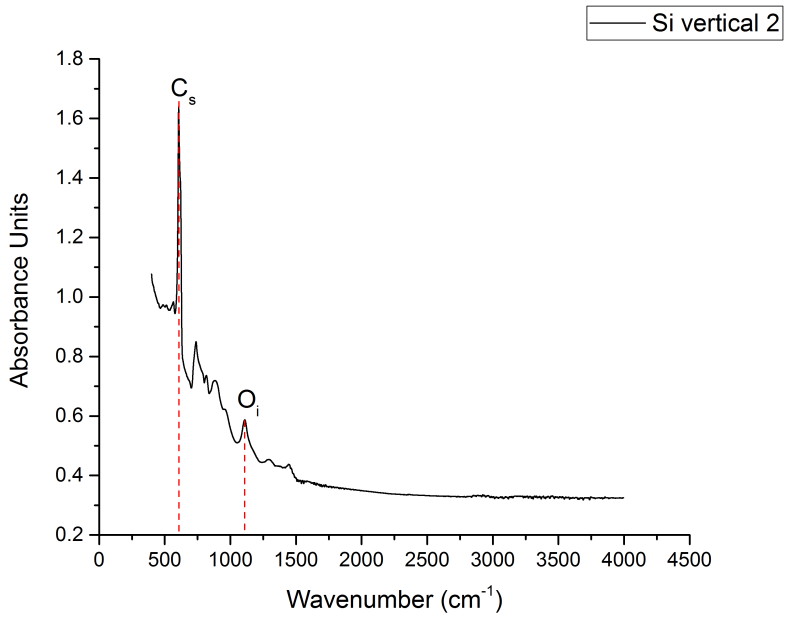

Figure 3.9: *The absorbance peak of O_i and C_s highlighted in the FTIR spectra at 1107 and 605 cm^{-1}.*

The quantitative analysis of these impurities has been done following the ASTM

F 1391-92 method for C_s and DIN 50438-1 A (93) method for O_i [46]. In both cases a reference sample made of a float-zone silicon was used. The reference sample absorbance spectrum, known to be without any detectable C_s and O_i, has been first multiplied by the thickness ratio of the test and reference samples and then converted to transmittance spectrum $Tr_{reference} = 10^{-Abs}$. The result was divided to the sample spectrum in order to obtain a comparison spectrum. A baseline created fitting the minimum points of the investigated peak was used to calculate the difference in height at the peaks wavenumber, see figure 3.10. The value Δh is finally used in accordance with the respective standard [46] to derive the concentration values of C_s and O_i.

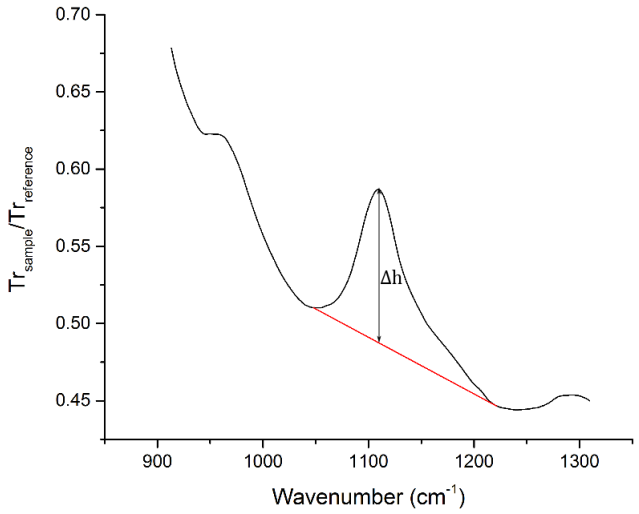

Figure 3.10: *Height difference in a comparison spectrum for the FTIR concentration calculations of Oxygen.*

3.5 GDMS Measurements

GDMS measurements were performed at the Department of Materials Science at NTNU using the Thermo Scientific^{TM} ELEMENT GD^{TM} PLUS GD-MS. Argon was used to ion sputter the sample surface with a discharge gas flow of 400 ml/min, discharge voltage of 800 V and current 60 mA. The sample holder had a diameter of 22 mm while the analyzed area was ~8 mm with a sputtering rate of 20 nm/sec. The ionized atoms, removed from the sample surface, were absorbed by the mass spectrometer using a magnet designed for mass range 2-260 u and with ppt detection limit. Finally the selected mass per charge ratio, see section 2.4.1, is analyzed by the detector system equipped with an automatic switching between different detection modes, see figure 3.11.

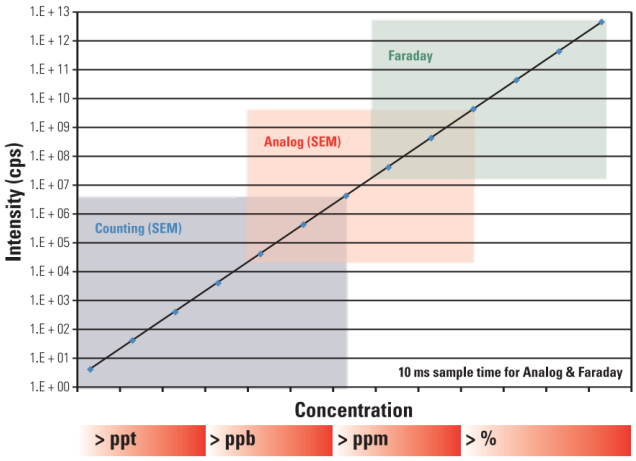

Figure 3.11: *Dynamic range of the detection system of Thermo Scientific^{TM} ELEMENT GD^{TM} PLUS GD-MS [37].*

Figure 3.11 describes the three detectors used, Faraday cup, analog secondary electron multiplier (SEM) and counting (SEM), according with the concentration level of the element under investigation.

The concentration calculations start from the intensities in counts per second (cps) of the impurity and silicon isotopes, evaluated in the ion beam ratio (IBR):

$$IBR = \frac{I_i/A_i}{I_{Si}/A_{Si}} \tag{3.1}$$

where I_i and I_{Si} are the intensities of the impurity and silicon selected isotopes with relative abundance of, respectively A_i and A_{Si}. A relative sensitivity factor (RSF), depending on elements and instrument settings (for this machine and application [47] was used), is then applied to calculate the impurity concentration (C_i) in ppbw, calculated as:

$$C_i = 10^9 \cdot IBR \cdot RSF_i \tag{3.2}$$

First the vertical samples were cut in smaller pieces to fit in the 22 mm sample holder. The analysis procedure then started with a peak calibration using a metallic grade silicon sample with deliberate addition of many elements in ppm range. Afterwards a highly pure sample was analyzed to find the interference peaks and remove residual elements from the first measurement. Finally the vertical cut samples from both Si and SiGe ingots were analyzed at three heights (bottom, middle and top), see figure 3.12.

3.6 Transmittance Measurements

Transmittance measurements were conducted at the Department of Physics at NTNU using an Modernized Cary UV/Vis/NIR spectrophotometer. The light source used

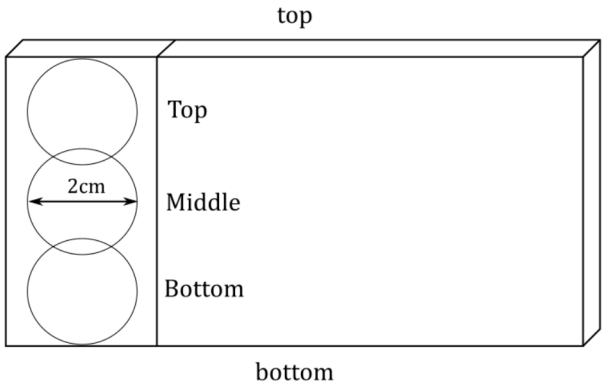

Figure 3.12: *Vertical cut sample sketch to describe the analyzed area with GDMS.*

for the experiments was a 150 W Tungsten lamp together with a prism plus gratings Cary double monochromator. The monochromatic light was directed to the sample and the transmitted component captured by an InGaAs photodiode. Finally the signal is converted from analog to digital and sent to the computer running OLIS 14 software. The samples analyzed were horizontally cut wafers DSP and considered to have a specular surface. The polishing was provided by VARIO Kristallbearbeitung.

The software OLIS 14 has been set to collect data in transmission mode using fixed HV with 150 increments in the range of wavelength between 950-1250 nm and 10 reads per datum. At the beginning of each experiment session a background spectrum without samples was collected and then subtracted to the samples spectra in order to measure the contribution of the wafers only. The measurements were performed on both Si and SiGe DSP wafers taken from bottom, middle and top of the ingots.

In order to be compared, the transmittance spectra of samples with different thickness needed to be calibrated to a common reference thickness, in this case 0.07 cm. To do so the transmittance spectrum is converted to absorbance through the relation $Tr_{reference} = 10^{-Abs}$. Since $Abs \propto$ thickness, the spectrum is multiplied by the thickness ratio between the sample and the reference. Finally the *Abs* spectrum is converted again to transmittance.

3.7 Integrating Sphere Measurements

The experiments were done at the Department of Physics at NTNU using a custom built integrating sphere designed by B. Smeltzer for his master thesis [40]. The setup is described in figure 3.13.

A halogen white light bulb source was used and directed trough the Carl Zeiss M4 QIII monochromator system equipped with a prism, as dispersive element, and an adjustable slit width, set at 0.5 mm. The Thorlabs Optical Chopper ML2000 was

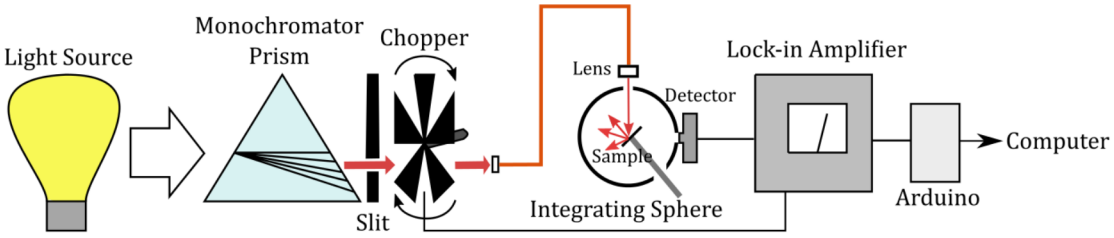

Figure 3.13: *Integrating sphere schematic setup.*

placed at the monochromator output port to create a modulated optical intensity signal of known frequency. A reference square signal, with the same frequency as the chopper rotation, was sent to the SR510 lock-in amplifier. The lock-in amplifier uses a principle, called phase-sensitive detection, to measure the amplitude of that particular frequency component present in the signal and filter noise from other surrounding light sources. Meanwhile, the monochromatic light was directed to the integrating sphere using an optical fiber and a Thorlabs A220TM-B lens to focus the light beam to the sample. The integrating sphere ports and sample position are shown in figure 3.14.

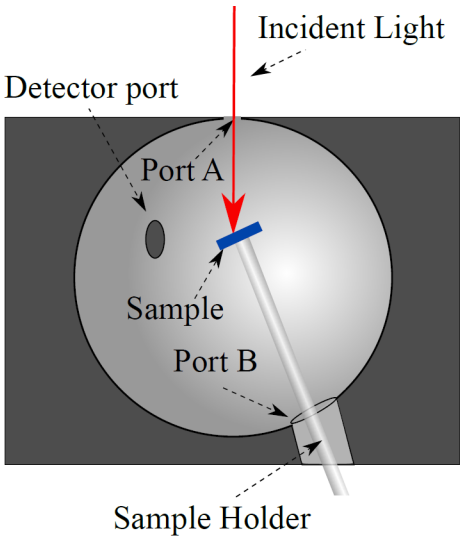

Figure 3.14: *A diagram of the integrating sphere with ports (labeled A and B) for the incident light and sample, as well as a detector port [40].*

Looking at figure 3.14 the sphere has three ports: A for the incoming light beam, B for the sample holder and the detector port. The design of the sphere is a trade off between wall flux ($\propto$ detector signal), and sphere multiplier factor (spatial

integration capability). A 45 mm sphere diameter with port diameters Port A = 2 mm, Port B = 9.0 mm, and Detector Port = 6.5 mm were chosen by B. Smeltzer as it maintained a small port fraction of <2% and a sphere efficiency factor of over twenty [40]. The sphere was fabricated out of aluminum by the NTNU machine shop and the internal walls of the sphere were coated with a white diffuse paint (Labsphere 6080). The detector used was a germanium photodetector Thorlabs PDA50B-EC, it converted the light intensity to DC current, amplified the signal by 30dB and sent it to the lock-in amplifier through a BNC cable. The incoming voltage was expanded again by the amplifier and feed to Arduino Mega2560 which digitized the signal and sent it to the computer through a USB cable. Python software was used to continually store the data in a text file for further analysis.

The measurements were set in the wavelength between 900-1400 nm with 10 nm steps between each point and 3 s of dweel time in which the data were acquired. A Zeber Stepper controller was used to change the selected wavelength of the monochromator. The analysis procedure started with the analysis of a reference sample of known reflectance ∼0.97. Afterwards the samples in table 3.2 were tested and their spectra collected in text files in order to be analyzed later using OriginPro 2016. Based on the substitutional method explained in section 2.4.4 and equation 2.22, ρ_s of each sample was calculated. In this thesis, since the samples are also transmitting light, this value does not include only the reflectance but also the transmittance and will be described as $(Ref + Tr)$ from now on.

3.8 SEM Measurements

A tabletop SEM Hitachi TM3000 has been used during the characterization sessions in the NanoLab's cleanroom at NTNU. Since the samples were composed of a non conductive material, such as glass, it was necessary to cover the surface with a layer of conductive material using the sputter coater Cressington 208 HR B to avoid charging. The coating material used in this work was Pt/Pd (80/20) with a thickness of 4 nm.

The sample was placed on the sample stage using a carbon tape and placed at a working distance of $\backsim$ 8 mm. Image mode was performed with a 15kV voltage to collect BSE, with particular attention on compositional contrast, as explained in section 2.4.5. Hitachi TM3000 software has been used for images acquisition.

4

Results and Discussion

In this chapter the experimental results will be presented in different sections according with the particular method used. In each section a discussion is carried out to compare the collected values to the literature and to the other techniques sections, in order to give a satisfactory description of the trends found.

4.1 GDMS

4.1.1 Impurities Concentration

As mentioned earlier, the samples analyzed using GDMS were the two vertical cuts of Si and SiGe ingots. The concentrations have been calculated at three heights (bottom, middle and top) using the equation 3.2 and values in table 4.1. the detection limit (DL) and RSF values are specific of the Thermo Scientific^{TM} ELEMENT GD^{TM} PLUS GD-MS at NTNU.

Element	**Atomic Mass [u]**	**RSF**	**Abundance [%]**	**DL [ppbw]**
B	11	0.6	80.10	6.6
Al	27	0.7	100.00	4.5
Si	28	–	92.23	–
Ti	48	0.5	73.72	0.2
Fe	56	0.9	91.75	0.9
Ni	58	0.7	68.07	0.6
Cu	63	0.9	63.00	1.6
Ge	74	1	36.28	–

Table 4.1: *The table illustrates atomic mass and abundance of the elements analyzed, together with their RSF and DL according to [47].*

The impurities concentrations in ppbw of the analyzed elements are collected in figure 4.1 for the SiGe ingot and figure 4.2 for the Si one. These values are the

average of three consecutive measurements, the standard deviations (SD) of each position are listed in table 4.2 and included in the error bars in figures 4.2 and 4.1.

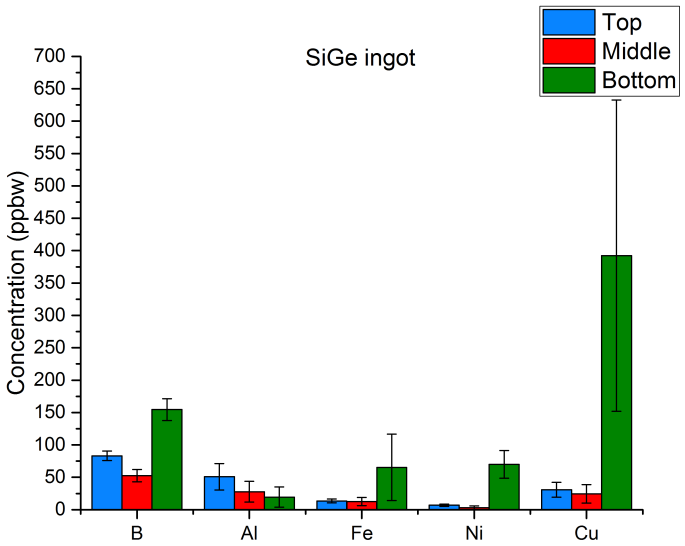

Figure 4.1: *Concentrations in ppbw of the impurities from top to bottom of the SiGe ingot. The error bars show the standard deviation for each average value.*

	Si [ppbw]			SiGe [ppbw]		
Element	**top**	**middle**	**bottom**	**top**	**middle**	**bottom**
B	75 ±3	57±2	49±2	83±7	53±9	155±17
Al	18 ±1	7 ±1	4 ±1	51 ±20	28 ±16	19 ±16
Fe	61 ±10	1 ±1	2 ±1	14 ±3	12 ±6	65 ±51
Ni	24 ±5	4 ±4	9 ±1	7 ±2	3 ±3	70 ±21
Cu	51 ±12	15 ±5	11 ±2	31 ±12	24 ±14	392 ±240

Table 4.2: *The table illustrates the average value of the three measurements made at each position and their standard deviation.*

Ti was also analyzed during the measurements but no detectable concentration was found, therefore it is not included in the graphs showing the results. Ge concentration are semi quantitative values because no RSF was available for this element.

Discussion

The two graphs in figure 4.2 and figure 4.1 show that the impurities level in the SiGe ingot is higher than in the Si one, especially Cu concentration, which is increased of

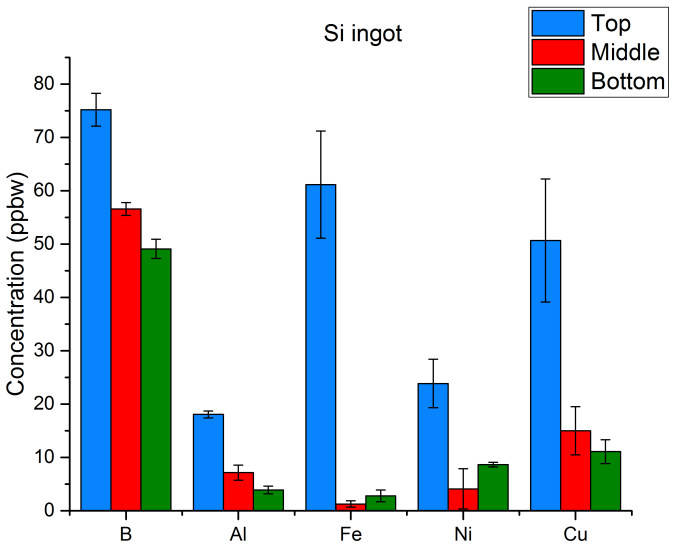

Figure 4.2: *Concentrations in ppbw of the impurities from top to bottom of the Si ingot. The error bars show the standard deviation for each average value.*

eight times. This difference between the two ingots can be explained by the purity level of Ge (99.999%). The addition of a third component in the melt, after Si and B, increases the chances of contamination, and Cu, Fe and Ni are typical metal bases that can be found in the Ge powder.

For what concerns the concentration trends, based on section 2.3.2 about segregation and table 2.1, all the elements under investigation have a partition coefficient $k_0<1$ or $k_0<<1$ and they should segregate towards the ingot's top during the solidification process [48]. This is true for the Si ingot, as can be seen in figure 4.2, where the metallic impurities segregate to the top of the ingot following a curve, according to Scheil equation 2.11, that is steeper the smaller the k_0 coefficient. Therefore B, which has a $k_0 = 0.8$, has a concentration increase less pronounced than Fe or Ni, for example, which have a $k_0 = 8 \cdot 10^{-6}$. The slightly higher concentration of Fe and Ni in the bottom compared to the middle is a known effect of crucible/coating contamination [49].

A different behavior is instead described by the SiGe ingot, here the values at the bottom are the highest for all the elements except Al. Looking at table 4.2 it can be noted that the standard deviation of values in the last measurement is suddenly increased to a degree that could partially explain the abnormal results at the bottom. The higher variation of values was found to be related to a drop in Si signal during the measurement. Taking into account the precarious nature of the results in this case, a research of similar high transition metal concentration at the bottom was carried out. A possible description of this precipitation mechanism was developed in [50] [51]. Buonassisi et al. analyzed the co-precipitation mechanisms of transition

metals in silicon and observed the formation of mixed-metal silicide systems at temperature close to 1400°C. They proposed that these systems may have formed via a liquid–alloy intermediate phase, driven by the presence of Cu, which is believed to facilitate the precipitation of Ni and Fe through grain boundaries. Therefore the unintentional addition of Cu, as impurity element in the Ge powder, could have caused the formation of an intermediary liquid system (droplet), that precipitating through the Si bulk has adsorbed other metals via solid–liquid segregation. This idea could also explain why Al is not following the same trend since it is not part of the mix of metals described in [50]. It is not clear though if the presence of Ge in the Si lattice has facilitated the process, which did not occur in the Si ingot, or it was only a function of Cu concentration. In [52] the idea that Ge-vacancy complexes can facilitate metal gettering is developed, arguing in favor of the first option. More about the Ge-vacancy theory is explained in the following section about FTIR results. Further analysis at the bottom of SiGe should have been carried out but for lack of time it was not possible to do so. If the high concentration is confirmed, a possible future research could be focused on the assessment of Ge contribution in the precipitation mechanism.

4.1.2 Ge distribution in SiGe

The Ge concentration has been analyzed using GDMS with the same procedure explained above. The semi quantitative results are shown in figure 4.3 together with the ideal distribution calculated using Scheil equation 2.11 and an initial concentration of 1%. The standard deviation for these measurements was stable around 0.05% and is represented in the error bars of figure 4.3.

Discussion

The average concentration is found to be 1.07% which is in good agreement with the concentration intentionally added when the ingot was prepared. This result can be used as a confirmation of the reliability of the measurements. Also the distribution of Ge in the vertical direction is found to be in accordance with Scheil equation and the segregation theory of section 2.3.2.

4.2 FTIR

The concentrations of C_s and O_i were calculated, as explained in section 3.4.1, at five positions along the height of the two ingots using the vertical cuts. The standards ASTM F 1391-92 for C_s and DIN 50438-1 A (93) method for O_i ensure to give an accuracy of ± 0.1 ppma [46].

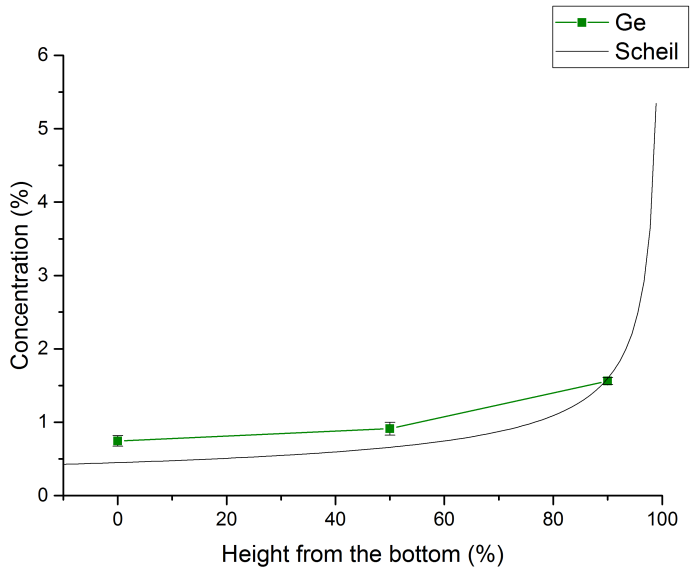

Figure 4.3: *Ge distribution through the ingot height compared to the distribution predicted using Scheil equation.*

4.2.1 C_s Concentration

The C_s concentrations along the vertical axis in the Si and SiGe ingots are shown in comparison in figure 4.4.

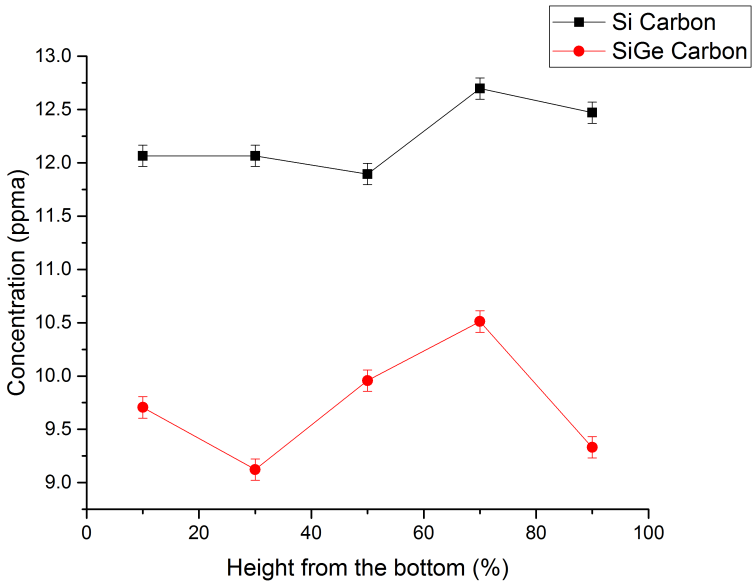

Figure 4.4: *C_s concentration comparison between the Si and SiGe ingots.*

Discussion

The results in figure 4.4 show that the concentration of carbon is relatively high, 12 ppma in Si and 10 in ppma in SiGe, compared to typical values for mc-Si. These results were expected because the particular furnace used to cast the ingots showed, already in previous castings, a tendency to C contamination, probably due to residual presence of oxygen in the chamber during the solidification process. This oxygen excess is connected to the Ar flow being not fully optimized [53]. As explained in section 2.3.2, oxygen can react with the graphite heaters to produce CO(g), which will diffuse in the melt and contaminate the crystal with carbon atoms. The k_0 coefficient for C is 0.07 and therefore a segregation to the top was expected. The trend is instead of slight increase for Si and oscillating for SiGe. This behavior can be explained, according to [27] and [54] by the high concentration of C in the melt. The two papers cited describe how Si ingots with a C concentration close to the solubility level, $5 \cdot 10^{18}$ atoms/cm^3, are already saturated with C at the beginning of solidification and they use the concentration of $4 \cdot 10^{17}$ at the bottom of the crucible as confirmation for this assumption. Since in this thesis the concentration at the bottom is exceeding that value, $5 \cdot 10^{17}$ for SiGe and $6 \cdot 10^{17}$ for Si, it is concluded that the same mechanism of [27] is occurring. If the carbon concentration exceeds the local solubility limit, excessive carbon precipitates as SiC and C_s, the only carbon detectable with FTIR, does not follow Scheil's equation [54]. If the total amount of C was detectable, it would probably fit the segregation curve. The presence of SiC precipitates are known to be detrimental for mc-Si efficiency, but a slow cooling process as the one used in this thesis, could, through melt flows, carry the SiC to the periphery of the crucible [54], reducing its concentration in the most important parts of the ingot. Further analysis should be carried out to asses if this is the case for the ingots examined.

Comparing the two ingots, instead, it can be highlighted that SiGe concentration of C_s is 1 $\pm$0.01 ppma lower than in Si. This difference could be related to the increased precipitation of oxygen when Ge is included in the lattice, which is going to be described in the next section, carbon behavior in fact is strictly connected to the oxygen one since they co-precipitate [55].

4.2.2 O_i Concentration

The O_i concentrations along the vertical axis in the Si and SiGe ingots are shown in comparison in figure 4.5 together with their ideal distribution according to Scheil's equation. In the calculation of Scheil's equation a $k_0 = 1.25$ was used, see table 2.1, and the initial concentration C_0 was calculated as the average of the five values measured.

Discussion

The first thing to notice in figure 4.5 is the good agreement between the measured values trend and the one predicted by Scheil's equation for both the ingots. Inter-

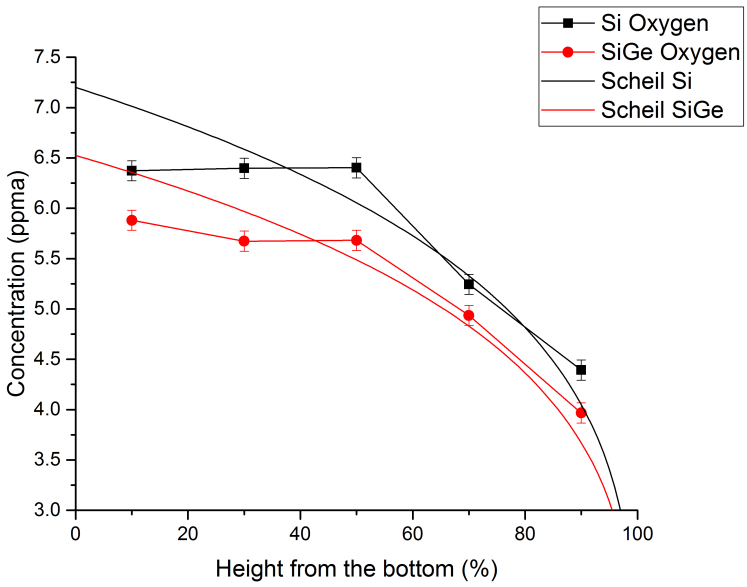

Figure 4.5: *O_i concentration comparison between the Si ingot, SiGe ingot and their ideal Scheil distribution.*

stitial oxygen is usually mostly present at the bottom and decreases towards the top [55], the results confirm this behavior and show that the presence of Ge in the lattice does not influence it.

The second important information that can be deduced from figure 4.5 is that the O_i concentration is reduced of 1 $\pm$0.1ppma in the SiGe ingot. The property of SiGe to reduce interstitial oxygen concentration has been widely studied for Czochralski (CZ) grown monocrystal silicon ingots [7] [10]. In these studies the inclusion of Ge in the lattice has been used to reduce the B-O defects which are related to the light induced degradation (LID) of carrier lifetime, due to their high recombination activity. In their work M. Arivanandhan et al. [7] described the effect of Ge in the Si lattice and how this could effect the O_i precipitation. Ge atoms induce compressive elastic strains, see figure 4.6, in the Si lattice due to the larger radius of germanium (1.22 Å) compared to that of silicon (1.17 Å) [7].

The local lattice strain could drive the formation of Ge-vacancy pairs or vacancy-O complexes to reduce the energy strain. The main effect of these complexes is to reduce void formation in the Si lattice and the related void nucleation in exchange of single/smaller voids. This theory fits very well with the characteristics of the SiGe ingot studied in this thesis. The O_i is then reduced because oxygen grows as precipitates during post-growth cooling of the ingots by using Ge-vacancy defect complexes as nucleation centers [7]. Moreover, the metal gettering, revealed by the GDMS results, could be related to the Ge-vacancy pair as pointed out in [52]. The implication of this strain effect could have positive repercussions on many different levels of the mc-Si material, from the increase of carrier life time, to the more homo-

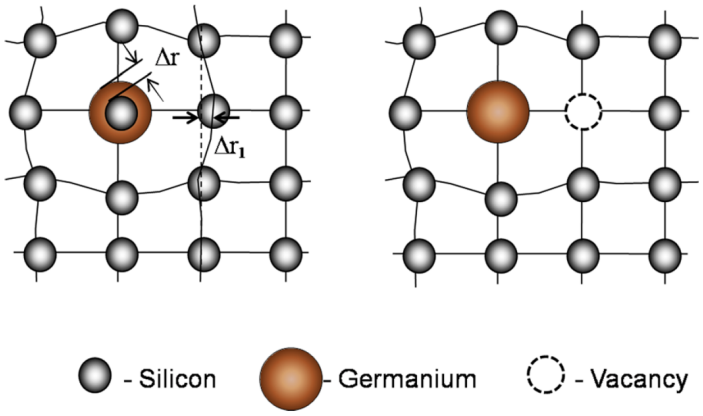

Figure 4.6: *Two-dimensional schematic view of the strained lattice of Ge doped Si, on the left. Schematic view of the Ge-vacancy pair in the Si lattice, on the right [7].*

geneous dislocation density [56], to the precipitation of metal impurities. Further analysis of the dislocation density, carrier lifetime and gettering on these two ingots could give some interesting insights on the mechanism described above.

4.3 FPP

The resistivity of the two ingots was assessed using the horizontal cuts at three heights (bottom, middle and top) in the way described in section 3.3. The average results and their standard deviation are listed in table 4.3.

4.3.1 Resistivity

Sample	**Resistivity** [Ω·**cm**]
Ge_3	0.80 ± 0.05
Ge_15	0.98 ± 0.08
Ge_25	1.04 ± 0.05
Si_3	0.78 ± 0.03
Si_15	1.03 ± 0.07
Si_25	1.18 ± 0.12

Table 4.3: *The table illustrates the average resistivity and standard deviation of the seven measurements made for each wafer.*

The values have been plotted in figure 4.7 to better show and compare the resistivity trend from bottom to top of both the ingots.

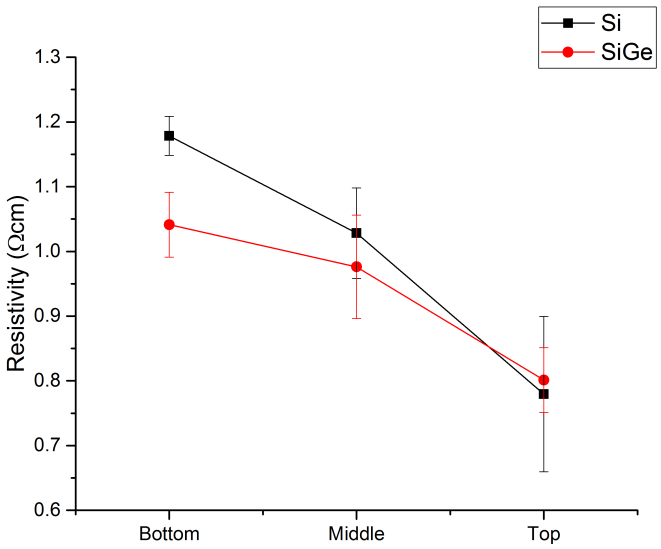

Figure 4.7: *Resistivity results plotted from bottom to top of Si and SiGe ingots. The error bars show the standard deviation for each average value.*

Discussion

Looking at table 4.3 it can be noted that, although varying slightly from position to position, the two ingots have a resistivity around 1 Ω·cm. This results is in good agreement with the concentration of B doping intentionally added during the production process. As earlier explained in section 2.1.2, it is possible to engineer the material conductivity (σ), and therefore the resistivity ($\rho = 1/\sigma$), trough the introduction of precise amounts of impurity elements. Equation 2.4 shows that σ is directly proportional to the carrier densities (n and p). Doping the material with a density of B atoms (N_A), that outnumber the carrier density at room temperature ($\sim 10^{10}$ cm^{-3}), it is possible to approximate $n \simeq N_A$ and $N_A >> p$. At this point N_A can be calculated in order to achieve a resistivity of 1 Ω·cm, which is ideal for solar application. Using a hole mobility value for Si of 410 cm^{2}V^{-1}s^{-1} the dopant density was found to be $1.5 \cdot 10^{16}$ cm^{-3}. The smaller resistivity values for SiGe can also be explained by equation 2.4 because this time the hole mobility increases with Ge concentration in SiGe alloy [58].

From figure 4.7 an immediate conclusion is that the resistivity is decreasing moving to the top of the ingot, in both cases. As described above, ρ is inversely proportional to the concentration of B. The resistivity trend is suggesting that B concentration should increase from the bottom to the top. Looking at figures 4.2 and 4.1, that are showing the concentration of boron in Si and SiGe, it is possible to notice that the expected variation is confirmed in the Si case but not in SiGe. This discrepancy in the concentration of boron and resistivity trends in SiGe can be

explained through the effect of electrically active oxygen precipitates, the thermal donor described in section 2.3.2, which act in the opposite way of B atoms. The presence of both donor and acceptors give rise to a compensation mechanism [45] which leads to an increase in resistivity. In section 4.2.2 it has been assumed that the reduction in interstitial oxygen was related to its precipitation through Ge-vacancy defects, therefore in SiGe there should be a higher concentration of oxygen precipitates. Following this idea, knowing that the electrically active oxygen clusters and SiO_2 precipitates will be concentrated at the bottom, it is possible to argue that the resistivity is a result of B and oxygen thermal donors interaction. The higher ρ at the bottom would then be caused by compensation of donors and acceptors while the middle and top values are following the relation with boron. A future analysis of oxygen precipitates in the SiGe ingot can better validate this theory.

4.4 Transmittance Measurements

The transmittance measurements have been performed following the procedure described in section 3.6 for the horizontal DSP wafers at three heights (bottom, middle and top) four times for each sample to assess the reproducibility. The average results are collected in figure 4.8. Their standard deviations were found stable along the studied wavelengths and are listed as percentage of the signal value in table 4.4 for illustrative reasons. The numeration of the samples goes from top to bottom.

Sample	**SD** [%]
Ge_2_DSP	0.1
Ge_14_DSP	0.2
Ge_26_DSP	0.4
Si_2_DSP	0.1
Si_14_DSP	0.9
Si_26_DSP	0.2

Table 4.4: *The table illustrates the standard deviation of the four measurements made for each wafer. They are expressed as percentage of the signal values in the transmittance spectra.*

Discussion

Looking at figure 4.8 a series of information about how the wafers interact with light can be derived. First of all the step shape of the transmission curve is related to the bandgap energy of the material. Recalling section 2.1.1, silicon is an indirect semiconductor with E_g= 1.12 eV, which, using equation 2.1, corresponds to a wavelength of 1100 nm. Light will theoretically stop to be absorbed and start to be transmitted by silicon at ∼1100 nm but, because of its indirect bandgap, this step occurs at a smaller wavelength and it is clearly visible in figure 4.8. Looking at

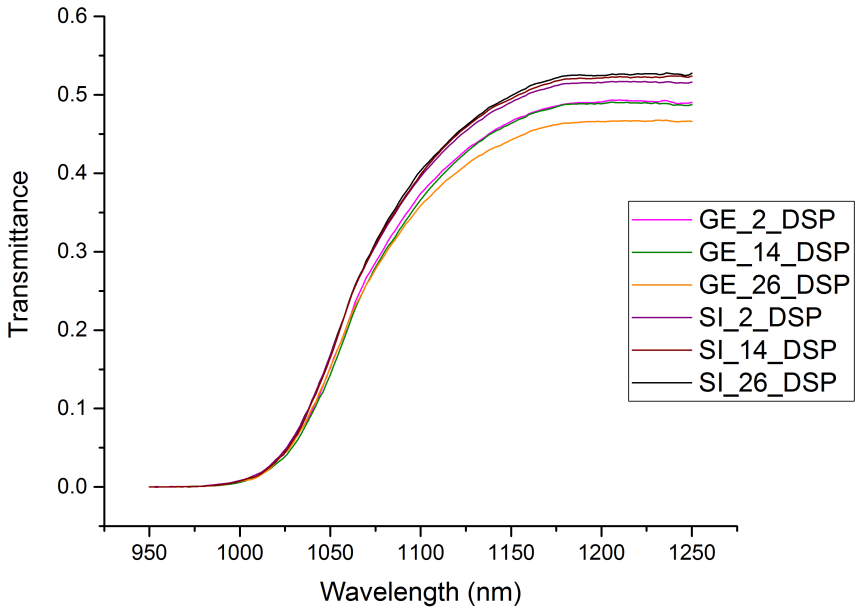

Figure 4.8: *Transmittance spectra of the six wafers examined using OLIS spectrophotometer.*

the different heights in Si, no noticeable change occurs, as expected. On the other hand it has been shown in section 4.1.2 that varying the height in SiGe increases the Ge concentration from the bottom to the top. Germanium has a lower energy bandgap (0.67 eV) compared to silicon, therefore, introducing Ge in the Si lattice, the alloy's E_g is going to decrease proportionally to the Ge percentage. In figure 4.8 this variation in bandgap between the different Ge concentrations, from 0.75% at the bottom to 1.5% at the top, is not detectable. The bandgap difference can be calculated as $Si_{1-x}Ge_x$ $1.12 - 0.41x + 0.008x^2$ eV [57], resulting 1.1136 eV at the top, 1.1162 eV at the middle and 1.1169 eV at the bottom. This changes are not high enough to produce appreciable variations in the measurements under investigation.

The key result of this experiment is the different behavior of Si and SiGe wafers. The transmittance curve of SiGe is less steep and slightly shifted towards the infrared region of the light spectrum. This behavior represents the higher capacity of SiGe to excite EHP at longer wavelengths thanks to the smaller energy bandgap and confirms the potential increase of photocurrent that can be achieved using SiGe in solar cells.

4.5 Integrating Sphere

The results that will be shown in this section are related to the measurements performed on the samples listed in table 3.2. The experiments were done three times for each sample to asses the reproducibility. The absorption spectra were calculated using a reference sample as $Abs = 1 - Ref - Tr$, with $Ref + Tr = \rho_s$ given by equation 2.22 in section 2.4.4. The averaged values were then plotted in figures 4.9 and 4.10, in which the standard deviations are represented by the shaded regions. Before any analysis, though, it should be highlighted that the accuracy of these results depends on a combination of the slit width, which affects the wavelength by a factor ± 30 nm, and the angle of incidence of light, which was varying due to difficulties in positioning the samples. This inaccuracy is also noticeable in figures 4.9 and 4.10.

4.5.1 Si and SiGe wafers

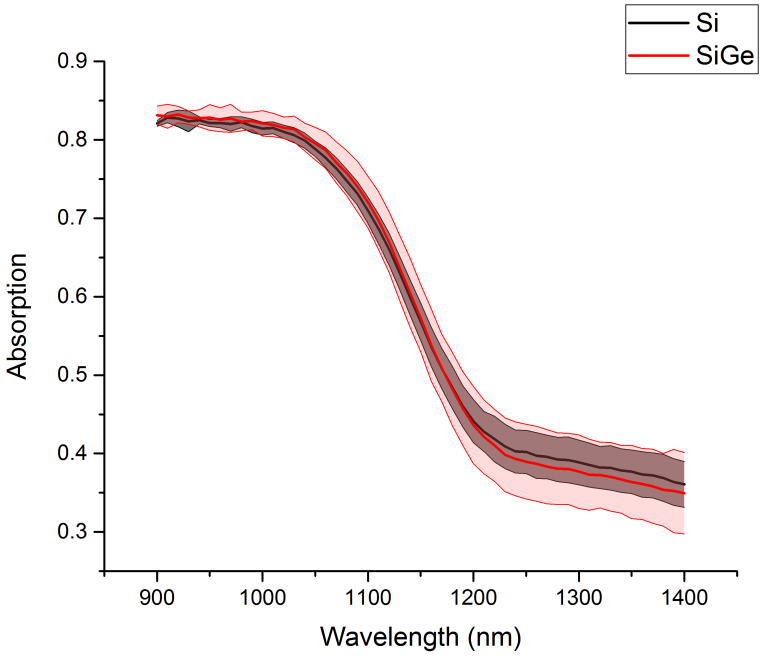

Figure 4.9: *Absorption spectra of the Si and SiGe wafers examined using the integrating sphere. The shaded regions represent the standard deviation range.*

Discussion

Even though the absorption spectra are affected by the inaccuracy constraints described, they can still give important qualitative information about the samples. In

figure 4.9 a comparison between Si and SiGe wafers is carried out. The two curves describe again the cutoff region close to the bandgap wavelength, as described for the transmittance spectra in section 4.4. It is visible also in this case that the SiGe wafer continues to absorb light at longer wavelengths, shifting the curve step to the right, confirming that SiGe alloy can increase the usable region of the light spectrum.

Looking at the initial and final part of the curves in figure 4.9, the values stabilize at around 0.85 and 0.35. From [59] and the transmittance curves in figure 4.8, it is possible to conclude that, for a DSP Si surface at wavelengths < 1100 nm, $Tr = 0$ and $Ref \simeq 0.3$; while at wavelengths > 1100 nm, $Tr \simeq 0.5$ and $Ref \simeq 0.5$. Knowing that $Abs = 1 - (Tr + Ref)$, the theoretical values of absorption at the beginning and end of figure 4.9 should be 0.7 and 0. The variation of 0.15, at small wavelengths, can be explained as an effect of surface roughness for the sample examined compared to the DSP, on which the theoretical values are based. The rough surface can increase the yield of light absorbed by the wafers because the rays are reflected back and forth between the inclined surfaces [59]. This effect is used, for example, in etching and texturing of solar cells. The final absorption variation is instead more complicated to explain, since the band-to-band transitions in Si and SiGe is negligible at long wavelengths, such as 1300 nm. An hypothesis, based on the work of R. Santbergen et al. [59], is that free carriers absorption plays an important role when the dopant concentration increases. Even though the total dopant concentration in this case is lower than [59], since the ingots examined are from the top of the ingot, the boron concentration is high enough to partially explain the absorption observed. The integrating sphere, then, is also reflecting light on the sample multiple times, increasing the probability of free carrier absorption to happen. Summing these two effects, the long wavelength behavior can be understood but a better investigation is needed to confirm the hypothesis.

4.5.2 Annealed and Not Annealed Fibers

Discussion

In this section the samples analyzed are substantially different from all the other samples presented in the thesis, therefore it is necessary to pay particular attention when comparing these results to the previous ones. From figure 4.10 only a qualitative comparison, due to the inaccuracy problems previously described, can be carried out between the annealed and not annealed SiGe fibers. It is clear that the not annealed sample follows a less steep cutoff curve than the annealed one and absorbs more in the longer wavelength region. This behavior can be explained analyzing the differences between the two types of fibers.

Even though they both have been produced using the molten core fiber drawing method and the same Ge% in the SiGe alloy, the annealed fibers have undergone a further treatment, which has modified how the Ge concentration is distributed in the fiber [36]. The high temperature gradient, imposed by the CO_2 laser on the silica cladding, melted the semiconductor core, then, translating the fiber, the molten zone was moved through the rod leaving the solidified crystal behind. According to the

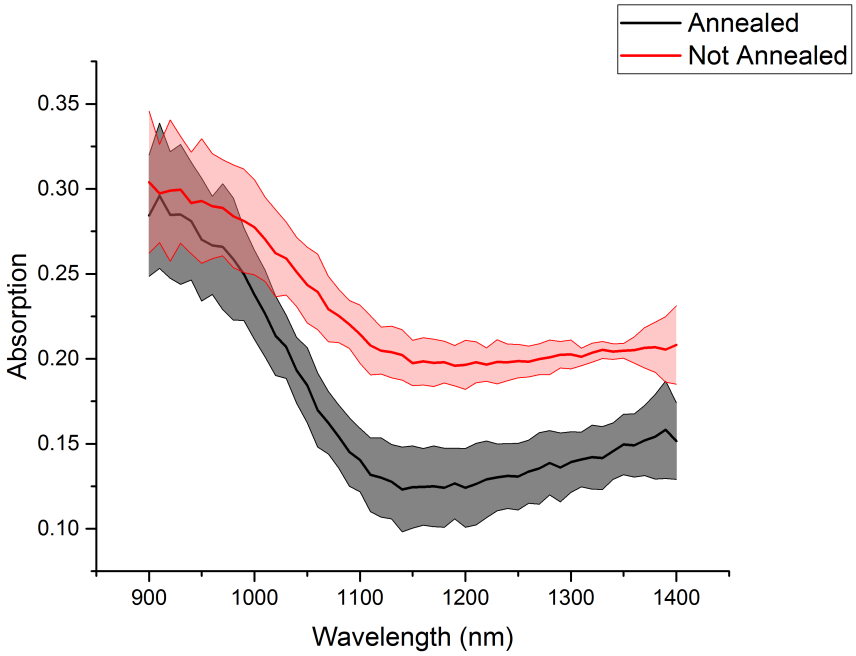

Figure 4.10: *Absorption spectra of the annealed and not annealed microwires arrays examined using the integrating sphere. The shaded regions represent the standard deviation range.*

solidification theory, in section 2.3, and the zone refining method in section 2.3.4, it is possible to predict that the composition distribution of Ge after the treatment will have an initial and final transient with a steady-state region in between. To prove this assumption of homogeneity for the annealed samples compared to the not annealed ones, SEM BSE images have been used. Thanks to the properties of BSE explained in section 2.4.5, it is possible to gain compositional information from figures 4.11 and 4.12.

As shown in the theory, Ge, which has an higher atomic number compared to Si, will give rise to a higher signal and hence look brighter in the image. In figure 4.12 the brighter regions are then assumed to be Ge rich regions, which are occurring randomly along the fiber, as expected due to the production process and previous studies [36]. The annealed fiber instead, in figure 4.11, does not present brighter regions and therefore the semiconductor core is assumed to have an homogeneous concentration of Ge.

The variation in the composition distribution of Ge is, then, the only difference between the two samples arrays used to collect the spectra in figure 4.10 and can be used to describe the curves differences. The sharper drop off in the annealed sample's curve can be explained due to a better defined bandgap, corresponding to 6% Ge in silicon, compared to the not annealed sample, which, instead, has different bandgaps in different regions. These bandgaps variations can then be

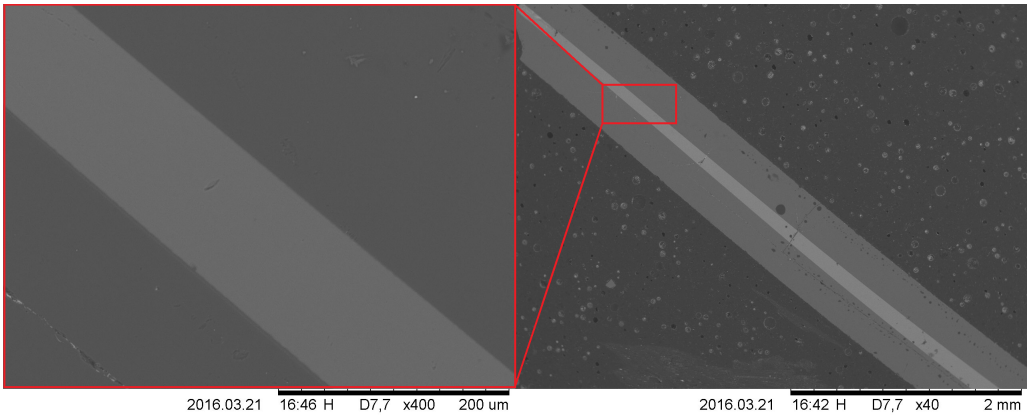

Figure 4.11: *Image of the longitudinal section of the SiGe annealed sample collected using an SEM BSE detector and 15kV acceleration voltage. The same sample is observed at 400x and 40x magnification.*

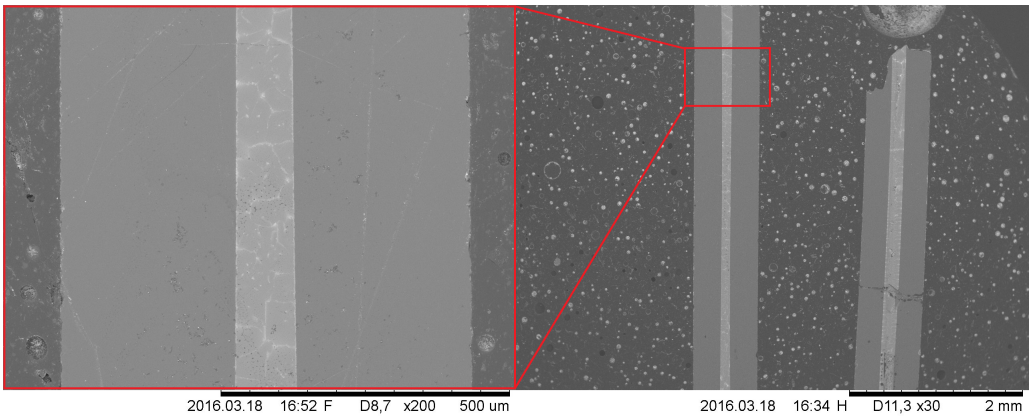

Figure 4.12: *Image of the longitudinal section of the SiGe not annealed sample collected using an SEM BSE detector and 15kV acceleration voltage. The same sample is observed at 200x and 30x magnification.*

connected to the start of absorption at longer wavelengths for the not annealed sample. The absorption peak is then reached more slowly because different regions absorbs different wavelengths and smooth the overall behavior. Looking at the last part of the curves, in the long wavelength region, the not annealed sample has higher absorption values. This behavior can be related to the free carriers absorption described in the section before. The absorption is helped by internal scattering within the wires, due to inhomogeneous SiGe concentration [14] and combined with trapping of light in the silica cladding. This enhanced absorption in inhomogeneous microwires could be used to develop new microwire-based solar cells but more data is needed to confirm the findings.

5

Conclusion

The use of SiGe alloy and microwire geometries are attractive solutions to produce innovative solar cells with higher light absorption, lower purity requirements and less material usage. In this thesis the effect of germanium in silicon for solar applications has been studied comparing a mc-Si ingot and a mc-SiGe ingot with 1% of Ge content. The experimental results have shown that the Ge concentration distribution in the SiGe ingot follows the expected trend, defined by Scheil's equation for an initial concentration of 1%. This value was also confirmed by the GDMS result of 1.07% average Ge concentration in the ingot. From the same experiment the SiGe ingot has shown higher impurity levels than Si, probably due to metal bases contamination from the Ge powder used in the casting process. The metallic impurities were mostly found in the bottom of the ingot suggesting that a precipitation mechanism has taken place in the SiGe case. A possible explanation has been found in the formation of mixed-metal silicide systems via a liquid-alloy intermediate phase driven by the high concentration of Cu, which is believed to precipitate through the grain boundaries carrying also Fe and Ni. It is yet not clear if Ge atoms in the crystal lattice are facilitating the process through Ge-vacancy complexes. Interstitial oxygen measured using FTIR resulted to be lowered by 1 ppma in the SiGe ingot, confirming that previous findings in mono-SiGe can be applied in this mc-SiGe case. Utilizing the same method carbon is found to be exceeding the solubility limit in silicon in both the ingots but with a lower concentration of C_s in the SiGe one. The lower concentration of O_i and C_s is suspected to be related again to the Ge-vacancy complexes, which are formed to release the compressive elastic strain energy imposed by the lattice variation due to Ge atoms in the lattice. Carbon and oxygen are then supposed to co-precipitate using Ge-vacancy pairs as nucleation centers. Concerning the electrical properties, the resistivity values are found to be in accordance with the density of boron, intentionally added during the casting process, to achieve 1 Ω·cm. Even though the trends of B concentration and resistivity in the SiGe ingot are not following their theoretical relation, a possible explanation is found due to compensation mechanisms at the bottom between oxygen precipitates, acting as donors, and B atoms, acting as acceptors. Further analysis of oxygen precipitates are necessary to confirm this theory. Finally the transmittance and

absorption measurements have shown as expected that SiGe is absorbing slightly more than Si in the infrared region due to a small reduction of energy band gap. An overview on the possibility of increasing light absorption in inhomogeneous SiGe microwires has been carried out trough integrating sphere absorption analysis. The microwires were composed by a SiGe core with 6% of Ge concentration embedded in a silica cladding. They have been produced using the molten core fiber drawn method. These fibers were then divided by an additional annealing process using a CO_2 laser. The homogeneity of the annealed samples and inhomogeneity of the not annealed ones was assessed using SEM BSE images. The integrating sphere results confirm that the fibers with micro-compositional variations are absorbing more in the infrared region and reaching the absorption peak more slowly than the homogeneous ones. This behavior is suspected to be related to the differences in bandgap energies between the regions with high and low Ge concentration. These findings could lead to new microwire-based solar cells systems but more data is needed to confirm the hypothesis.

Overall it is found that SiGe is a valuable solution to increase solar cells conversion efficiency, thanks to enhanced absorption of light in the infrared region and to improved material quality, through Ge-vacancy complexes generation. The micro-compositional variations in SiGe microwires have also shown an interesting capability of absorbing light in the infrared region, confirming previous findings and attracting attention for future research in this direction.

5.1 Further Work

The results of this thesis have shown several points in which more investigations and analyses are required to better explain the mechanisms involved. First of all the effect of germanium in the transition metals precipitation, shown by GDMS results, could be an interesting starting point for a future project. Si and SiGe ingots with different Cu concentrations, intentionally added to the melt, can be studied to see if the precipitation will occur in both cases at the same Cu concentration. The differences can give valuable insights on the effect of Ge-vacancy complexes described in this thesis. At the same time an analysis on O_i and C_s concentration could be carried out to connect the two precipitation phenomena in one more comprehensive picture. Due to lack of time it was not possible to double check the B concentration variation in the SiGe ingot and it should be done. If the trend is confirmed an analysis of oxygen precipitates at the bottom of the sample could give the information necessary to explain the discrepancy between resistivity and B concentration trends found in this work. Finally the results from the SiGe inhomogeneous microwires have shown promising light absorption capacities. An interesting research can start by this assumption and, if verified by more, and more accurate, data it could lead to the design of a new microwire-based solar cell system with increased light absorption and reduced material usage.

Bibliography

[1] G. Masson, S. Orlandi, Becquerel Institute, *EPIA Global Market Outlook for Photovoltaics 2015-2019*, 2015.

[2] A. Goetzberger, C. Hebling, and H. Schock, *Photovoltaic materials, history, status and outlook*, Materials Science and Engineering, 2003.

[3] Shockley W. and Queisser H. J., *Detailed Balance Limit of Efficiency of pn Junction Solar Cells*, J. Appl. Phys, 1961.

[4] Tina Enright, *SiGe: a key to unlocking the potential of solar cells*, Photovoltaics Bulletin, Elsevier, october 2003.

[5] H. Stöhr and W. Klemm, *Über zweistoffsysteme mit germanium. i. germanium/ aluminium, germanium/zinn und germanium/silicium.*, Zeitschrift für anorganische und allgemeine Chemie, 1939.

[6] N. Usami, Y. Azuma, *SiGe bulk crystal as a lattice-matched substrate to GaAs for solar cell applications*, Applied Physics Letters 77, 2000.

[7] M. Arivanandhan, R. Gotoh, T. Watahiki, K. Fujiwara, Y. Hayakawa, S. Uda and M. Konaga, *The impact of Ge codoping on the enhancement of photovoltaic characteristics of B-doped Czochralski grown Si crystal*, Journal of Applied Physics 111, 2012.

[8] S.W. Boettcher, J.M. Spurgeon, M.C. Putnam, E.L. Warren, D.B. Turner-Evans, M.D. Kelzenberg, J.R. Maiolo, H.A. Atwater, N.S. Lewis, *Energy-Conversion Properties of Vapor-Liquid-Solid–Grown Silicon Wire-Array Photocathodes*, Science 327, 2010.

[9] F.A. Martinsen, B.K. Smeltzer, J. Ballato, T. Hawkins, M. Jones, and U.J. Gibson, *Horizontally aligned silicon microwires as solar cells*, Optics Express Vol. 23, 2015.

[10] X. Yu, P. Wang, P. Chen, X. Li and D. Yanga, *Suppression of boron–oxygen defects in p-type Czochralski silicon by germanium doping*, Applied Physics Letters 97, 2010.

[11] J. Su, G. Zhong, Z. Zhang, X. Zhou, X. Huang, *Influence of germanium doping on the performance of high-performance multi-crystalline silicon*, Journal of Crystal Growth, 2015.

[12] K.Nakajima, N.Usami, K.Fujiwara, Y.Murakami, T.Ujihara, G.Sazaki, T.Shishido, *Growth and properties of SiGe multicrystals with microscopic compositional distribution for high-efficiency solar cells*, Solar Energy Materials & Solar Cells 73, 2002.

[13] W.Pan, K.Fujiwara, N.Usami, T.Ujihara, K.Nakajima, R.Shimokawa, *Ge composition dependence of properties of solar cells based on multicrystalline SiGe with microscopic compositional distribution*, Journal of Applied Physics 96, 1238 (2004).

[14] M. Tayanagi, N. Usami, W. Pan, K. Ohdaira, K. Fujiwara, Y. Nose, and K. Nakajima, *Improvement in the conversion efficiency of single-junction SiGe solar cells by intentional introduction of the compositional distribution*, Journal of Applied Physics 101, 2007.

[15] J. Nelson, *The Physics of Solar Cells*, Imperial College Press, 2003.

[16] Ben G. Streetman, Sanjay Kumar Banerjee, *Solid State Electronic Devices*, sixth edition, 2009.

[17] Nakajima et al., *Growth and properties of SiGe multicrystals with microscopic compositional distribution for high-efficiency solar cells*, Solar Energy Materials & Solar Cells 73 305–320, 2002.

[18] *Standard Tables for Terrestrial Solar Spectral Irradiance at Air Mass 1.5 for a 37 deg. Tilted Surface, E892-87*, American Society for Testing and Materials, Annual Book of ASTM Standards, Philadelphia, PA.

[19] *Standard Tables for Terrestrial Direct Normal Solar Spectral Irradiance for Air Mass 1.5, E891-87*, American Society for Testing and Materials, Annual Book of ASTM Standards, Philadelphia, PA.

[20] M. A. Green, *Solar Cells - Operating Principles, Technology and System Applications*, Prentice-Hall, 1982.

[21] P. Kofstad and T. Norby, *Defects and Transport in Crystalline Solids*, Compendium Defect Chemistry and Reactions, University of Oslo, 2009.

[22] W. D. Callister, *Fundamentals of Materials Science and Engineering*, John Wiley & Sons, Inc., 2001.

[23] W. A Tiller, K. A Jackson, J. W Rutter, and B Chalmers, *The redistribution of solute atoms during the solidification of metals*, Acta Metallurgica, 1953.

[24] W. W. Mullins and R. F. Sekerka, *Stability of a planar interface during solidification of a dilute binary alloy*, Journal of Applied Physics, 1964.

[25] H. Fredriksson and U. Akerlind, *Solidification and Crystallization Processing in Metals and Alloys*, John Wiley & Sons, 2012.

[26] J. A. Burton, R. C. Prim, and W. P. Slichter, *The distribution of solute in crystals grown from the melt. part I. Theoretical*, The Journal of Chemical Physics, 1953.

[27] C. Reimann, M.Trempa, J.Friedrich, G.Möller, *About the formation and avoidance of C and N related precipitates during directional solidification of multicrystalline silicon from contaminated feedstock*, Journal of Crystal Growth 312, 2010.

[28] R. Hull, *Properties of Crystalline Silicon*, Institution of Engineering and Technology, 1999.

[29] M.A. Martoranoa, J.B. Netob, T.S. Oliveiraa, T.O. Tsubaki, *Refining of metallurgical silicon by directional solidification*, Materials Science and Engineering B 176, 2011.

[30] D. P. Brunco, M.0. Thompson, D.E. Hoglund, M.J. Aziz, H.J. Gossmann, *Germanium partitioning in silicon during rapid solidification*, J. Appl. Phys. 78 (3), 1995.

[31] K. Tang et al., *Critical assessment o the impurity diffusivities in solid an liquid silicon*, JOMS Journal of the Minerals, Metals and Materials Society, 2009.

[32] J. Lilliestråle, *Structural properties of Ge doped multicrystalline Silicon wafers and Solar cells*, Master Thesis NTNU, 2012.

[33] H.J.Möller, C. Funke, A. Lawerenz, S. Riedel, M. Werner, *Oxygen and lattice distortions in multicrystalline silicon*, Solar Energy Materials & Solar Cells 72, 2002.

[34] M. Di Sabatino, S.Binetti, J.Libal, M.Acciarri, H.Nordmark, E.J.Øvrelid, *Oxygen distribution on a multicrystalline silicon ingot grown from upgraded metallurgical silicon*, Solar Energy Materials & Solar Cells 95, 2011.

[35] A. Autruffe, *Silicon directional solidification, Impurity segregation and defects*, Doctoral Thesis NTNU, 2014.

[36] D. Coucheron, U. J. Gibson, *Rapid Directional Recrystallisation of SiGe Fibres*, Master Thesis NTNU, 2015.

[37] *http://www.thermoscientific.com/ElementGD*

[38] Thermo Nicolet Corporation,*Introduction to Fourier Transform Infrared Spectrometry*, 2001.

[39] A.Uhlir, *The Potentials of Infinite Systems of Sources and Numerical Solutions of Problems in Semiconductor Engineering*, Bell System Technical Journal, 1955.

[40] B. Smeltzer, *Optical Properties of Silicon Microwire Arrays for Photovoltaic Applications*, Master Thesis NTNU, 2015.

[41] B.A. Saleh and M.C. Teich, *Fundamentals of Photonics*, Wiley, 2007.

[42] Labsphere, *Integrating Sphere Theory and Applications. Technical Guide* Available: www.labsphere.com.

[43] Peter J. Goodhew, John Humphreys, Richard Beanland, *Electron Microscopy and Analysis*, CRC Press, 2001.

[44] J. Ballato, T. Hawkins, P. Foy, B. Yazgan-Kokuoz, C. McMillen, L. Burka, S. Morris, R. Stolen, R. Rice, *Advancements in semiconductor core optical fiber*, Optical Fiber Technology, 2010.

[45] K. Austad, *Characterization of electrical activity and lifetime in compensated multicrystalline silicon*, Master Thesis NTNU, 2011.

[46] BRUKER OPTIK, *OPUS software manual*, 2005.

[47] M. Di Sabatino, A.L. Dons, J. Hinrichs, L. Arnberg, *Determination of relative sensitivity factors for trace element analysis of solar cell silicon by fast-flow glow discharge mass spectrometry*, Spectrochimica Acta Part B 66, 2011.

[48] M.P. Bellmann, E.A.Meese, L.Arnberg, *Impurity segregation in directional solidified multi-crystalline silicon*, Journal of Crystal Growth 312, 2010.

[49] T. Buonassisia, A.A. Istratova, M.D. Picketta, J.P. Rakotoniainab, O. Breitensteinb, M.A. Marcusc, S.M. Healdd, E.R. Weber, *Transition metals in photovoltaic-grade ingot-cast multicrystalline silicon: Assessing the role of impurities in silicon nitride crucible lining material* Journal of Crystal Growth 287, 2006.

[50] T. Buonassisi, M. Heuer, A.A. Istratov, M.D. Pickett, M.A. Marcus, B. Lai, Z. Cai, S.M. Heald, E.R. Weber, *Transition metal co-precipitation mechanisms in silicon*, Acta Materialia 55, 2007.

[51] T. Buonassisi, M.A. Marcus, A.A. Istratov, M. Heuer, T.F. Ciszek, B. Lai, Z. Cai and E.R. Weber, *Analysis of copper-rich precipitates in silicon: Chemical state, gettering, and impact on multicrystalline silicon solar cell material*, J. Appl. Phys. 97, 2005.

[52] J. Chen, D. Yang, X. Ma, W. Wang, Y. Zeng and D.Que, *Investigation of intrinsic gettering for germanium doped Czochralski silicon wafer*, Journal of Applied Physics 101, 2007.

[53] Ursula Gibson, Marisa Di Sabatino and Antoine Autruffe, *Private communications.*

[54] L. Liua, S. Nakanoa, K. Kakimoto, *Carbon concentration and particle precipitation during directional solidification of multicrystalline silicon for solar cells*, Journal of Crystal Growth 310, 2008.

[55] H.J. Möller, L. Long, M. Werner, and D. Yang, *Oxygen and Carbon Precipitation in Multicrystalline Solar Silicon*, phys. stat. sol. (a) 171, 175, 1999.

[56] M.P. Bellmann, T.Kaden, D.Kressner-Kiel, J.Friedl, H.J.Möller, L.Arnberg, *The impact of germanium doping on the dislocation distribution in directional solidified mc-silicon*, Journal of Crystal Growth 325, 2011.

[57] C.G. Van de Walle and R.M. Martin, *Theoretical calculations of heterojunction discontinuities in the Si/Ge system*, Phys. Rev. B 34, 5621, 1986.

[58] C.K Maiti, G.A Armstrong, *Applications of Silicon-Germanium Heterostructure Devices*, pg 113, CRC Press, 2010.

[59] R. Santbergen, R.J.C. van Zolingen, *The absorption factor of crystalline silicon PV cells: A numerical and experimental study*, Solar Energy Materials & Solar Cells, 2007.

[60] J. Schilz and V. N. Romanenko, *Bulk growth of silicon-germanium solid solutions*, Journal of Materials Science: Materials in Electronics, 1995.

[61] P.R. Griffiths, James A. De Haseth, *Fourier Transform Infrared Spectrometry*, Wiley-Interscience, 2007.